POLITECNICO DI TORINO

Facoltà di Ingegneria

Corso di Laurea in Ingegneria Aerospaziale

Tesi di Laurea Magistrale

Development of CFD simulation methods to resolve acoustic characteristics of flow

Relatore:

Prof. Renzo Arina

Supervisore Aziendale:

Ing. Naveen Indolia

Candidato:

Jacopo Rossi Ferrini

Marzo 2021

Summary

Noise emitted from motor vehicles has been proven to have a major impact on human health. Since people are used to interact with motor vehicles on a daily basis, many authorities have been established all over the world with the purpose of regulating and monitoring the noise levels. Therefore, nowadays noise attenuation is considered with great care by many vehicle manufacturers.

Scania, which is a truck and bus manufacturer, always aim to be a benchmark when it comes to developing sustainable transport solutions and one of the major challenges for its internal combustion engines vehicles concerns the minimization of the noise emitted. The exhaust silencer serves this function for the engine unit and it is desired to have a high degree of performance. Often the acoustic performance of the exhaust silencer are computed ignoring the influence of flow-generated noise. This could lead to have large discrepancies between the real life performance and the simulations results. Therefore a simulation method which take into account the flow when computing the silencer acoustic performance is needed. Eventually, this could facilitate the development of Scania's next generation of exhaust systems.

The objective of this Master's thesis is to study the development of a CFD simulation method to resolve the acoustic characteristics of flow. In particular it will be shown how to properly set up direct noise calculation using the commercial software STAR-CCM+. Additional details of the thesis aim will be provided in chapter 1.

Then, in chapter 2 it will be reported a summary of all the basic theory concepts that are related the most with the topic discussed in this thesis work, including all the relevant metrics that has been used throughout this report.

In chapter 3 the main challenges associated to the set up of acoustic simulations in STAR-CCM+ will be described and a series of guidelines on how to solve these difficulties will be provided.

In chapter 4 the simulation method set with these guidelines will be validated. In particular, it will be shown that the obtained simulation results relate quite well with the available experimental data. Therefore, it will be concluded that STAR-CCM+ is a great tool for the analysis of simple silencer configurations either with or without flow.

Once the method has been validated, the simulations of real silencers geometries will be described in chapter 5. From the analysis of the results it will be inferred that the method yields accurate results even if used with complex silencer geometries. In addition, the comparison between the acoustic performance of the different silencers simulated will be presented and it will be shown which configuration is the most promising concerning flow-noise attenuation.

Finally, in chapter 6 the main conclusions will be summarized and ideas to further develop this thesis work will be presented.

Acknowledgements

This Master's Thesis project has been carried out in collaboration with the NXPS group at Scania CV AB. First of all, I would like thank all the members of the group for always helping me and making me feel welcome throughout this whole experience. It has been truly a pleasure to work in such a friendly environment. Furthermore, I would like to express my deepest gratitude to the engineer Naveen Indolia, my supervisor, for the continuous encouragement, the countless insights and the constant interest you have showed regarding my thesis. I really admire the enthusiasm and care you all put into your work and this motivated me to do my best.

I would also like to thank my professor at Politecnico di Torino, Renzo Arina, who has examined my thesis and has followed me during all my experiences abroad.

Special thanks must be given to my whole family for all the affection and teachings I have received throughout my entire upbringing. Without your help, I would not have been able to accomplish anything I have done.

Finally, I would also like to thank all the fellow students that I have had the pleasure of meeting during these long five years of university. Oddly, sharing all the stressful exams, confusing lectures and difficult assignments with you made the memories of my university period nearly pleasant.

Table of Contents

List of Tables

List of Figures

Chapter 1

Introduction

Noise pollution has been defined as the distressing noise that may harm the physical/mental activity of human being as well as animal life, [1]. It has already been shown that high levels of noise can have a severe effect on the human body, even if for a short period of time. As a matter of fact hearing loss is known to be caused by several factors but the most common are ageing and exposure to noise. Noise induced hearing loss depends on both the noise level and exposure duration. Namely the greater the noise level and/or duration, the greater the loss. Noise exposure has been shown to be associated with other health problems as well. Indeed, not only noise can be partly responsible for hearing impairments, but it can also affect blood circulation. This could eventually lead to hypertension, coronary heart disease and myocardial infarctions, [2]. Less severe but definitely more common is the impact that unwanted sounds might have on the annoyance of people. The day-evening-night average noise level is a parameter that has been shown to correlate well with community annoyance. This can be seen in Figure 1.1, where the percentage of highly annoyed people has been reported as a function of L_{den}. Since these data have been obtained from a survey conducted among different communities it can be concluded that also non-acoustic factors, such as demographic and culture can influence the perceived noise annoyance.

In addition, noise pollution is not only a threat for humans but it has a great impact on wildlife as well. As a matter of fact the noise generated by humans can affect the way some species of animals communicate with each other, hunt and mate, see [3] for an example.

Transportation, industry or recreational activities are common sources of unwanted sound and contribute greatly to the increase of noise pollution experienced nowadays. Furthermore, since world population is constantly increasing it can also be imagined that if noise pollution were to be ignored there would be a drastic increase in the near future. This is why several authorities have been established all over the world with the purpose of regulating and monitoring the noise levels.

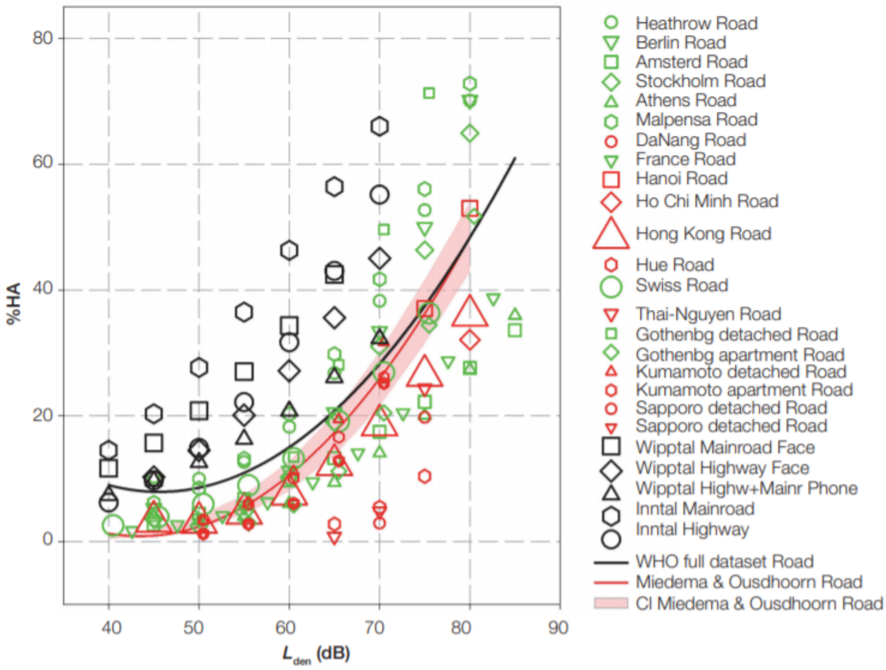

Figure 1.1: Scatterplot and quadratic regression of the relationship between road traffic noise (L_{den}) and annoyance (%HA), [4]

1.1 Heavy Truck Noise Sources

Since people are used to interact with road vehicles an a daily basis, their noise emission has a great impact on the quality of their life. This led many vehicles manufactures, such as Scania, to consider noise attenuation with great care. On a road vehicle there exist several sound sources, the relative power of which depends on both the vehicle type and the operating conditions. Generally the following sources can be identified:

- Powertrain noise
- Rolling noise
- Structure born noise
- Aerodynamic noise

Minimization of the noise level is one of the greatest challenges for internal combustion engine powered vehicles. The exhaust silencer serves this function for the engine unit and it is desired to have a high degree of performance. Usually a truck is equipped with a four-stroke engine and its main source of noise is given by the ignition pulsation. This is due to the periodic opening of the exhaust of each cylinder. Therefore, in the frequency spectra this type of noise will appear at specific frequencies, also known as engine orders, which are multiples of the engine rotational speed. Since most of the noise radiated from the engine is concentrated at these frequencies is fundamental to design a silencer which is able to attenuate these engine orders. Nevertheless, nowadays the silencer performance have increased so much that other noise source generation mechanism are starting to contribute greatly to the overall noise radiated, namely shell noise and flow generated noise.

The shell noise is mainly transmitted through the sidewall of the silencer and is generated from the mechanical vibration and the internal pressure pulsation related to the engine. The radiation of this type of noise is dominated by the surface with the lowest thickness. Therefore employing a thicker structure could attenuate the surface radiation but the silencer would result to be both heavier and more expansive.

Flow-generated noise, also known as self-generated noise, is the source of sound which will be investigated throughout this report and is originated by the turbulent structures formed by the hot and high speed flow moving both through the complex silencer geometry and outside of it. Its contribution to the overall noise level increase rapidly with the flow speed. Therefore a simple way to reduce this type of noise would be to employ a larger cross-section which determines lower velocities of the flow in the exhaust pipes. Nevertheless, this solution would also lead to a reduction of both the engine-pulsation and surface-radiation noise damping plus less available space on the truck. It can be concluded that all the three noise source generation mechanisms mentioned in this section are relevant when developing a muffler and a compromise has to be made to find the optimal solution.

Usually these acoustic phenomena are too complex to be approached analytically and therefore they are generally analysed through experiments, [5]. Nevertheless, thanks to the increase in available computational power, also numerical approach are starting to become a viable way to study these noise generation mechanism. In particular Computational Fluid Dynamics (CFD) has already been proven to be a valid method to determine flow noise characteristics, yielding results that are comparable to experimental analysis, see [6] as an example.

1.2 Thesis Aim

Scania is always trying to diversify out noise reduction strategies and is currently looking at a way to manipulate the flow turbulence which could lead to an attenuation of the exhaust noise. This needs the development of simulation methods to facilitate the development of Scania's next generation exhaust system. The target of this Master Thesis project is to perform CFD simulations with the objective being the study of acoustic characteristics of flow. In particular the ability of the commercial software STAR-CCM+ to capture acoustic phenomena will be investigated by the validation of two simulation cases. Then the same methodology will be applied on real silencer geometries in order to study how flow generated noise could be attenuated by a proper manipulation of the flow.

Chapter 2

Theory Background

In this chapter it will be presented a general overview of all the basic theory concepts that are considered important in relation to this study. First of all, the most relevant notions of fluid dynamics will be introduced. Then, two type of really important flows will be described. Namely, turbulent flows and boundary layer flows. Finally, this chapter will be concluded with a summary on the basics of acoustic, including noise generated aerodynamically.

2.1 Fluid Dynamics

Fluid dynamics is a branch of fluid mechanics that deals with the flow of fluids, hence the study of liquids and gases in motion. The equations of motion describing the flow in a fluid are based on the three law of conservation of mass, momentum and energy. Nevertheless, to be able to describe these equations in a mathematical form the fluid is required to satisfy the continuum assumption. Namely, an infinitesimal volume of fluid should be large enough to contain a statistically meaningful number of molecules that make up the fluid but sufficiently small if compared to a characteristic length scale of the flow. If this condition is satisfied, a pressure p, a velocity u_i, a fluid density ρ and a temperature T can be associated to each point in space x_i at every time instant t. Then, assuming a right-handed coordinate system the governing equation of fluid motion can finally be expressed as follow:

$$\frac{\partial \rho}{\partial t} + \frac{\partial \rho u_i}{\partial x_i} = S_C \tag{2.1}$$

$$\frac{\partial \rho u_i}{\partial t} + \frac{\partial \rho u_j u_i}{\partial x_j} = -\frac{\partial p}{\partial x_i} + \frac{\partial \tau_{ij}}{\partial x_j} + S_{M_i} \tag{2.2}$$

$$\frac{\partial \rho e}{\partial t} + \frac{\partial \rho u_i e}{\partial x_i} = -p\frac{\partial u_i}{\partial x_i} + \tau_{ij}\frac{\partial u_i}{\partial x_j} + \frac{\partial}{\partial x_j}\left(\kappa\frac{\partial T}{\partial x_j}\right) + S_E \tag{2.3}$$

where S_C, S_{M_i} and S_E are the source terms for the equations of conservation of mass, momentum and energy respectively, τ_{ij} is the viscous stress tensor, e the internal energy and κ the thermal conductivity of the fluid. The subscripts i, j and k identify the component of the vectorial variable considered and according to Einstein notation a repeated index has to be interpreted as a sum over all the directions of the coordinate system.

For an isotropic Newtonian fluid, hence a fluid whose shear stress is linearly proportional to the velocity gradient in the direction perpendicular to the plane of shear, the viscus stress tensor can be defined according to this expression:

$$\tau_{ij} = \mu\left(\frac{\partial u_i}{\partial x_j} + \frac{\partial u_j}{\partial x_i}\right) - \frac{2}{3}\mu\frac{\partial u_k}{\partial x_k}\delta_{ij} \tag{2.4}$$

where μ is the dynamic viscosity and δ_{ij} is the Kronecker delta function which is equal to one if $i = j$ and zero otherwise.

Since the internal energy can be related to the temperature through the specific heat at constant volume c_v:

$$e = c_v T \tag{2.5}$$

the system of governing equations previously defined is made up of five equations (one for each component of the velocity plus the continuity and energy equations) but six unknowns (u_i, ρ, p and T). Therefore, one additional equation need to be introduced to make the system solvable, and this is the equation of state:

$$p = \rho R T \tag{2.6}$$

This equation relates the thermodynamic properties of a gas through its specific constant R.

For simple laminar flow cases analytical solutions of this set of partial differential equations do exist. For more complex problems, such as turbulent flows, an analytical solution is not possible and approximations need to be introduced.

2.2 Turbulent Flows

The occurrence of turbulent flows in nature and technology is a common event. For instance, in technology turbulent flows may be present in nozzles and pipes while in nature turbulence is knows to have a great impact on the behaviour of the geophysical scale flows, such as atmospheric or oceanographic flows.

Over the last several decades the interest in turbulent flows has always been strong. As a matter of fact, since turbulence is still an unsolved problem from both a physical and mathematical point of view, it is common that incorrect turbulence modelling lead to a wrong solution of the flow.

Laminar	**Turbulent**
layered	disordered
smooth	fluctuating
ordered	chaotic

Table 2.1: Laminar and turbulent flow main characteristics

In Table 2.1 the main characteristics that distinguish a laminar flow from a turbulent flow are summarized while Figure 2.1 shows the evolution of a flame from laminar to turbulent. From the color of the flame it can be concluded that in the laminar flame the combustion is clearly weaker if compared to the turbulent flame. This is due to the stronger intensity of the mixing introduced by the turbulent regime which leads to a higher temperature of the flame (blue flame). Furthermore, while the laminar flame appear to be both smooth and free from clear structures, the turbulent flame display a chaotic motion, but not random, and disordered structures (also known as eddies).

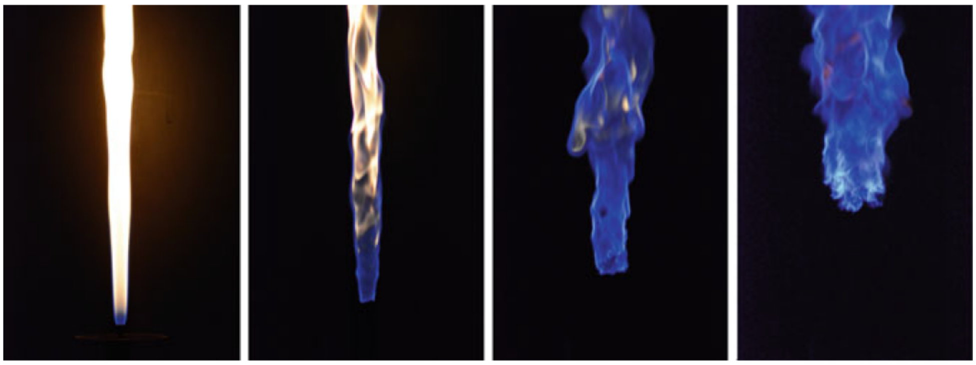

Figure 2.1: Laminar and turbulent flames, [7]

From these differences it may be thought that the laminar and turbulent regimes are governed by a different set of equations. Nevertheless, it has been shown that this is not true and at the present day it can be stated without any doubt that the equations of motion presented in the previous section are representative for both laminar and turbulent flows. Ideally, if the initial and boundary conditions were to be known with infinite accuracy, employing the governing equations it would be possible to predict the evolution of the flow field as a function of time.

A problem is defined to be well-posed only if the solution of a set of differential equations satisfy the following conditions:

- Existence of the solution
- The solution is singular
- Small disturbances in the initial and boundary conditions lead only to small variations of the solution

Nevertheless, in practice the initial and boundary conditions can be defined only until a certain degree of accuracy. It follows that a deterministic solution is achievable only for a well-posed problem. Namely, when the imperfections that are always present in the initial and boundary conditions are not able to affect the solution. This is the case for laminar flows. However, when the conditions for a well-posed problem are not satisfied, the solution becomes unpredictable, and this is what defines a turbulent flow. This means that for a given set of initial and boundary conditions defined with finite accuracy multiple solutions of a turbulent flow can be found. These solutions are often referred to as realizations of the turbulent flow. Therefore, when describing a turbulent flow, it comes natural to consider the statistics of the flow variables rather than the individual realizations.

Performing a turbulence experiment employing the same initial and boundary conditions would yield in principle a different realization every time. The ensemble average of a random variable ϕ is defined as follow:

$$\bar{\phi} = \lim_{N\to\infty} \frac{1}{N} \sum_{\alpha=1}^{N} \phi^{(\alpha)} \tag{2.7}$$

where the bar symbol identify the average operator, α is the index associated to every realization of the the experiment and N is the number of times the experiment has been repeated. Nevertheless, this definition is quite unpractical and usually the time average is used instead. As a matter of fact, when analysing a stationary process all single-point averages are independent of time and it can be concluded that both the ensemble and the time average would lead to the same result. Then, according to the Reynolds decomposition an arbitrary turbulence instantaneous variable ϕ can be separated into a mean flow quantity and its fluctuation:

$$\phi = \bar{\phi} + \phi' \tag{2.8}$$

In Equation 2.9 some useful operations which involves the application of the averaging operator are gathered.

$$\begin{aligned}
&(i)\ \ \overline{\phi'} = \overline{\psi'} = 0 && (ii)\ \ \overline{\overline{\phi}} = \overline{\phi} \\
&(iii)\ \ \overline{\frac{\partial \phi}{\partial s}} = \frac{\partial \overline{\phi}}{\partial s} && (iv)\ \ \overline{\phi + \psi} = \overline{\phi} + \overline{\psi} \\
&(v)\ \ \overline{\alpha \phi} = \alpha \overline{\phi} && (vi)\ \ \overline{\overline{\phi}\psi} = \phi \overline{\psi}
\end{aligned} \tag{2.9}$$

Here ϕ and ψ are fluctuating quantities while α is a constant.

For simplicity let's assume a non-stationary and incompressible flow with constant viscosity. In this case the energy conservation follows directly from the momentum conservation and both Equation 2.1 and Equation 2.2 can be simplified as follow:

$$\frac{\partial u_i}{\partial x_i} = 0 \tag{2.10}$$

$$\frac{\partial u_i}{\partial t} + \frac{\partial (u_i u_j)}{\partial x_j} = -\frac{1}{\rho}\frac{\partial p}{\partial x_i} + \nu \frac{\partial^2 u_i}{\partial x_j^2} \tag{2.11}$$

In both these equations the source terms have been neglected and the kinematic viscosity $\nu = \mu/\rho$ has been introduced. Then, after performing the Reynolds decomposition of the flow variables, the averaging operator can be applied to the decomposed equations and the following system can be found:

$$\frac{\partial \overline{u_i}}{\partial x_i} = 0; \quad \frac{\partial u_i'}{\partial x_i} = 0 \tag{2.12}$$

$$\frac{\partial \overline{u_i}}{\partial t} + \overline{u_j}\frac{\partial \overline{u_i}}{\partial x_j} = \frac{1}{\rho}\frac{\partial}{\partial x_j}\left[-\overline{p}\delta_{ij} + \mu\left(\frac{\partial \overline{u_i}}{\partial x_j} + \frac{\partial \overline{u_j}}{\partial x_i}\right) - \rho\overline{u_i' u_j'}\right] \tag{2.13}$$

These are the Reynolds Averaged Navier-Stokes equations which are often referred to as RANS equations.

It can be concluded that the employment of a linear decomposition method for the flow variables fail to decouple the mean flow quantities from their fluctuating part. As a matter of fact, inside Equation 2.13 it has appeared the new term $\rho\overline{u_i' u_j'}$ which is usually referred to as the Reynolds stress tensor. This term is responsible for the diffusion of the linear momentum of the average flow due to the fluctuations. Since the Reynolds stress tensor is symmetric, six new unknowns are introduced with this term and this lead to a closure problem.

A common approach to solve this problem is by approximating the Reynolds stress tensor such as to obtain a system were the number of unknowns equal the number of equations. Several approximations are based on the concept of the turbulent viscosity introduced by Boussinesq where the Reynolds stress tensor is modelled as follow:

$$-\rho\overline{u_i'u_j'} + \frac{2}{3}\rho k\delta_{ij} = \rho\nu_T\left(\frac{\partial\overline{u_i}}{\partial x_j} + \frac{\partial\overline{u_j}}{\partial x_i}\right) \tag{2.14}$$

In this equation ν_T represents the turbulent viscosity or eddy viscosity while k is the turbulent kinetic energy which is given by:

$$k = \frac{1}{2}\overline{u_i'u_i'} \tag{2.15}$$

Substituting Equation 2.14 inside Equation 2.13 it can be obtained:

$$\frac{\partial\overline{u_i}}{\partial t} + \overline{u_j}\frac{\partial\overline{u_i}}{\partial x_j} = \frac{1}{\rho}\frac{\partial}{\partial x_j}\left[-\left(\overline{p} + \frac{2}{3}\rho k\right)\delta_{ij} + \rho\nu_{eff}\left(\frac{\partial\overline{u_i}}{\partial x_j} + \frac{\partial\overline{u_j}}{\partial x_i}\right)\right] \tag{2.16}$$

where ν_{eff} is an effective viscosity made up of the sum of the kinematic viscosity and the turbulence viscosity. As a matter of fact, turbulent flows are known to be highly diffusive and dissipative and this effective viscosity relates well to this characteristic trait. Finally, with this approximation the number of additional unknowns is reduced from six to one, which is the eddy viscosity. Several turbulence model which calculates ν_T have been proposed in the past and here below a brief description of the most common can be found.

2.2.1 The k-ϵ Turbulence Model

In this turbulence model the turbulent kinetic energy k and the turbulent dissipation rate ϵ are used to calculate the eddy viscosity:

$$\nu_T = C_\mu\frac{k^2}{\epsilon} \tag{2.17}$$

Therefore, in order to close the system, the following two additional transport equations need to be introduced:

$$\frac{\partial k}{\partial t} + \overline{u_j}\frac{\partial k}{\partial x_j} = -\overline{u_i'u_j'}\frac{\partial\overline{u_i}}{\partial x_j} + \frac{\partial}{\partial x_j}\left[\left(\nu + \frac{\nu_T}{\sigma_K}\right)\frac{\partial k}{\partial x_j}\right] - \epsilon \tag{2.18}$$

$$\frac{\partial\epsilon}{\partial t} + \overline{u_j}\frac{\partial\epsilon}{\partial x_j} = -\frac{\epsilon}{k}\left(C_{\epsilon1}\overline{u_i'u_j'}\frac{\partial\overline{u_i}}{\partial x_j} + C_{\epsilon2}\epsilon\right) + \frac{\partial}{\partial x_j}\left[\left(\nu + \frac{\nu_T}{\sigma_\epsilon}\right)\frac{\partial\epsilon}{\partial x_j}\right] \tag{2.19}$$

Here, the Reynolds stress tensor $\rho\overline{u_i' u_j'}$ can be obtained from the manipulation of Equation 2.14 while the standard model constants can be found reported in Table 2.2.

C_μ	$C_{\epsilon 1}$	$C_{\epsilon 2}$	σ_ϵ	σ_k
0.09	1.44	1.92	1	1.3

Table 2.2: $k - \epsilon$ turbulence model standard constants, [8]

This model owes its popularity due to the low computational cost and it works well for external aerodynamic problems. Nevertheless, the $k - \epsilon$ model should only be applied to flows without strong pressure gradients, streamline curvature or separation, [9].

2.2.2 The $k - \omega$ Turbulence Model

This model always employs two scalar quantities for the calculation of the eddy viscosity but the specific dissipation rate $\omega = \epsilon/k$ is used instead of the dissipation rate ϵ:

$$\nu_T = \frac{k}{\omega} \tag{2.20}$$

As for the $k - \epsilon$ model two additional transport equations are needed to close the system, which are reported here below:

$$\frac{\partial k}{\partial t} + \overline{u_j}\frac{\partial k}{\partial x_j} = -\overline{u_i' u_j'}\frac{\partial \overline{u_i}}{\partial x_j} - \beta^* k\omega + \frac{\partial}{\partial x_j}\left[(\nu + \sigma^* \nu_T)\frac{\partial k}{\partial x_j}\right] \tag{2.21}$$

$$\frac{\partial \omega}{\partial t} + \overline{u_j}\frac{\partial \omega}{\partial x_j} = -\alpha\frac{\omega}{k}\overline{u_i' u_j'}\frac{\partial \overline{u_i}}{\partial x_j} - \beta\omega^2 + \frac{\partial}{\partial x_j}\left[(\nu + \sigma \nu_T)\frac{\partial \omega}{\partial x_j}\right] \tag{2.22}$$

Also in this case the Reynolds stress tensor has been modelled according to Equation 2.14 and the standard model constant have been reported in Table 2.3.

Generally, this model gives good results for boundary layer flows and for flows with strong pressure gradients and separation. Nevertheless, since it is very sensitive on inflow and free stream boundary conditions, the $k - \epsilon$ model is still recommended for external aerodynamic flows, [9].

α	β	β^*	σ	σ^*
5/9	3/40	9/100	1/2	1/2

Table 2.3: $k - \omega$ turbulence model standard constants, [10]

2.2.3 The SST $k-\omega$ Turbulence Model

The Shear Stress Transport (SST) $k-\omega$ turbulence model is based on the idea of joining the strengths of the $k-\omega$ and $k-\epsilon$ turbulence models. In this case the two transport equations are formulated as follow:

$$\frac{\partial k}{\partial t}+\overline{u_j}\frac{\partial k}{\partial x_j}=-\overline{u_i'u_j'}\frac{\partial \overline{u_i}}{\partial x_j}+\frac{\partial}{\partial x_j}\left[\left(\nu+\sigma^*\frac{k}{\omega}\right)\frac{\partial k}{\partial x_j}\right]-\beta^*\omega k \tag{2.23}$$

$$\begin{aligned}\frac{\partial \omega}{\partial t}+\overline{u_j}\frac{\partial \omega}{\partial x_j}=&-\alpha\frac{\omega}{k}\overline{u_i'u_j'}\frac{\partial \overline{u_i}}{\partial x_j}+\frac{\partial}{\partial x_j}\left[\left(\nu+\sigma\frac{k}{\omega}\right)\frac{\partial \omega}{\partial x_j}\right]-\beta\omega^2+\\&+2\left(1-F_1\right)\sigma_{\omega 2}\frac{1}{\omega}\frac{\partial k}{\partial x_j}\frac{\partial \omega}{\partial x_j}\end{aligned} \tag{2.24}$$

F_1 is a weighting function which is equal to one at the wall and zero near the edge of the boundary layer. This allow to switch between one model and the other depending on the distance from the wall. As a matter of fact, the model constants are expressed trough this relation:

$$\phi=F_1\phi_1+(1-F_1)\phi_2 \tag{2.25}$$

where ϕ_1 represents the values that all the model constants assume in proximity of the wall and ϕ_2 identify the values associated to the constants outside of the boundary layer. The turbulence viscosity is then calculated using this formula:

$$\nu_T=\frac{a_1 k}{\max\left(a_1\omega,\Omega F_2\right)} \tag{2.26}$$

where Ω stands for the vorticity magnitude and F_2 is another weighting function. The expression of both F_1 and F_2 as well as all the other model constants can be found in [11].

2.3 Boundary Layer

The boundary layer can be defined as the region close to a body where the flow is dominated by viscous effects and the relative velocity transition from zero, close to the wall, to the free stream condition. In Figure 2.2 it has been reported the development of the boundary layer over a flat plate immersed in a flow with free stream velocity V. As it can be seen the boundary layer initially start as laminar but then it transition to turbulent after a certain horizontal length. Inside the turbulent boundary layer a very thin region where the flow is laminar can still be distinguished. This region is called viscous sublayer. The transition from laminar to a fully turbulent state happens in the region called buffer layer.

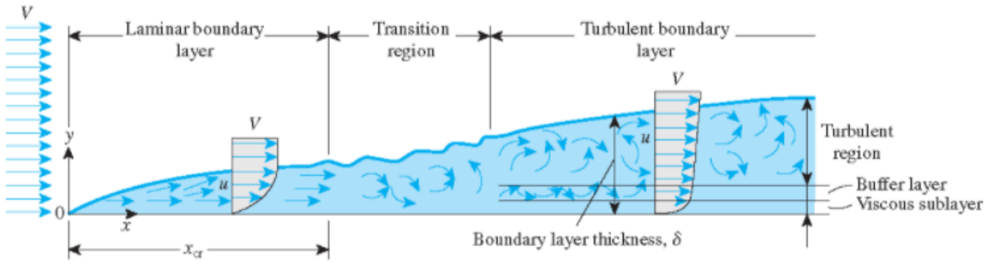

Figure 2.2: The development of the boundary layer for flow over a flat plate, [12]

A very important parameter that is often used when describing the velocity profile inside a boundary layer is the non-dimensional wall distance y^+. This quantity is given by the following formula:

$$y^+ = \frac{yu^*}{\nu} \tag{2.27}$$

where u^* represents the friction velocity and can be computed using these expressions:

$$u^* = \sqrt{\frac{\tau_w}{\rho}} \qquad \tau_w = \mu \frac{\partial u}{\partial y}\bigg|_{y-0} \tag{2.28}$$

It has been shown that inside the viscous sublayer ($y^+ < 5$) the velocity profile scales linearly with y^+ while in the turbulent region ($y^+ > 30$) it follows a logarithmic profile [7]. This notion is very useful when performing CFD simulations. As a matter of fact, in order to capture the very strong gradients present at the wall it is recommended to use a cell size which extends vertically less than $y^+ = 1$. Nevertheless, in a lot of situation this could lead to have a very large number of cells within the grid, which would increase the computational time considerably. Luckily, there exist wall functions which extrapolates the velocity profile inside the boundary layer exploiting the knowledge of the scaling law described before. Thus, a much coarser y^+ resolution can still be considered acceptable.

2.4 Fundamentals of Acoustics

Sound can be defined as a pressure disturbance propagating through a medium and it can be seen as a longitudinal wave. Namely the displacement of the particles induced by the acoustic pressure fluctuations is in the same direction of the wave propagation. Waves can be represented by wave fronts. These can be defined as surfaces where, at a given time, the particles displacement is everywhere the same. The lines perpendicular to wave fronts and pointing in the direction of the wave propagation are called sound rays. In Figure 2.3 both spherical and plane wave fronts have been reported with their respective sound rays.

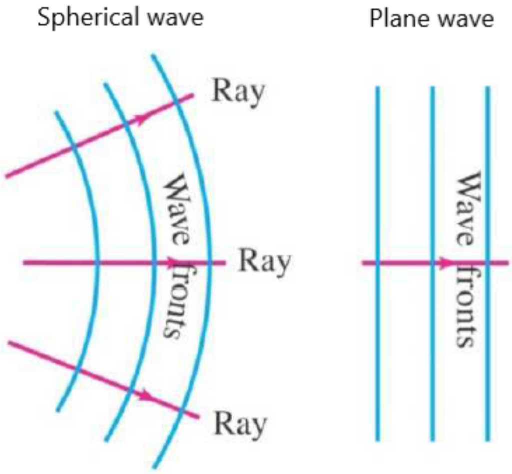

Figure 2.3: Wave fronts and sound rays of a spherical and plane wave, [13]

A sound source which radiate noise at a single frequency generates harmonic waves. A plane harmonic wave is the simplest type of wave and it can be easily described by this expression:

$$p'(x,t) = A\cos[\omega(t - x/c)] \tag{2.29}$$

where p' identify the acoustic pressure fluctuation, A is the wave amplitude, ω is the radial frequency ($\omega = 2\pi f$, f is the frequency in Hz) and c is the speed of sound. In Figure 2.4 it has been reported the sound pressure described by Equation 2.29 as a function of position for two time instants. It can be seen that between the two time instants the wave has travelled a distance ct towards the right. In the same picture also the wavelength λ has been pointed out. Since this length can be defined as the distance the wave have travelled during a period $T = 1/f$, the following important relation can be derived:

$$\lambda = cT = \frac{c}{f} \tag{2.30}$$

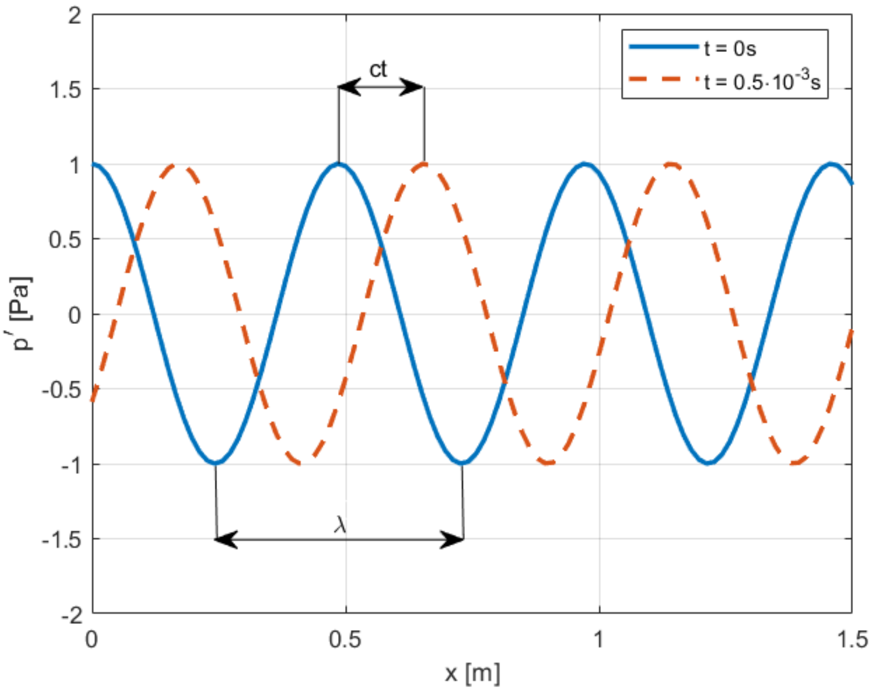

Figure 2.4: Pressure fluctuations of a plane wave with $f = 700$ Hz

The strength of a sound wave can be characterized by the following quantity:

$$p_e = \left[\frac{1}{T^*} \int_0^{T^*} \left[p'(t)\right]^2 dt \right]^{1/2} \tag{2.31}$$

which is often known as the effective sound pressure. In Equation 2.31 T^* has to be taken as a sufficiently long integration time, which is longer than the period of an harmonic wave T.

So far, only single frequency harmonic noise has been introduced. Nevertheless, in real life noise can be usually decomposed in a broadband component and a tonal one. The main difference is that for broadband noise the acoustic energy is spread over many frequencies, like for white noise, while for tonal noise it is concentrated around a single frequency. It is important to point out that the range of frequencies humans ears are able to resolve goes only from 20 Hz to 20 kHz.

Another relevant parameter that is often used when describing an acoustic field is the Sound Pressure Level (SPL). This can be calculated using the following relation:

$$\text{SPL} = 10 \log_{10} \left(\frac{p_e^2}{p_{e0}^2} \right) \tag{2.32}$$

and is expressed in decibel (dB). p_{e0} is the effective reference pressure and is often chosen as the human hearing threshold at 1000 Hz, which for air is $2 \cdot 10^{-5}$ Pa. The reason why this notation is usually preferred if compared to the effective sound pressure is due to the enormous range of values that the acoustic pressure may range. In Figure 2.5 it has been reported an order of magnitude of both the effective sound pressure and the SPL for different acoustic sources. As it can be seen while the effective sound pressure spans eight orders of magnitude the SPL is limited to two. It is worth noting that human ears are able to discern differences in SPL only if larger than 1 dB. Therefore, providing accuracies better than this would be meaningless.

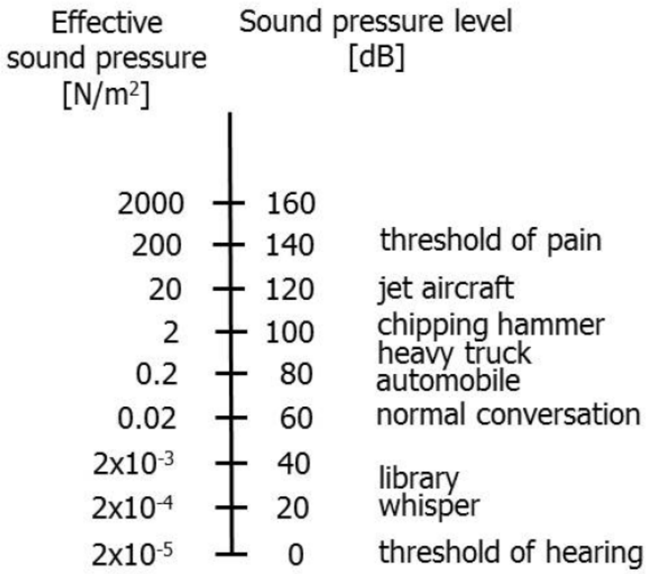

Figure 2.5: Typical p_e and SPL of different sound sources, [13]

2.4.1 The Wave Equation

It has been shown that, if viscous effects are neglected and sound is conceived as a very weak disturbance, the laws of conservation of mass, momentum and energy (section 2.1) can be rewritten in the following linearized form, [13]:

$$\frac{\partial \rho'}{\partial t} + \rho_\infty \frac{\partial {u_i}'}{\partial x_i} = 0 \tag{2.33}$$

$$\rho_\infty \frac{\partial {u_i}'}{\partial t} + \frac{\partial p'}{\partial x_i} = 0 \tag{2.34}$$

$$p' = c^2 \rho' \tag{2.35}$$

From these equations, after an easy algebraic manipulation, the 3D wave equation can be derived:

$$\frac{\partial^2 p'}{\partial x_i \partial x_i} - \frac{1}{c^2} \frac{\partial^2 p'}{\partial t^2} = 0 \tag{2.36}$$

Substituting Equation 2.29 inside the wave equation it can be proved that the plane harmonic wave is indeed a solution. If the same equation is then used in Equation 2.34 it can be found:

$$u' = -\frac{1}{\rho_\infty} \int \frac{\partial p'}{\partial x} dt = \frac{A}{\rho_\infty c} cos[\omega(t - x/c)] = \frac{p'}{\rho_\infty c} \tag{2.37}$$

Therefore, for a plane harmonic wave the pressure fluctuation and the particle velocity are in phase and can be related using the quantity $\rho_\infty c$ which is often called the characteristic acoustic resistance of the medium. Nevertheless, these consideration does not hold for all type of waves such as spherical waves.

Finally the sound intensity I which is defined as the acoustic energy per unit surface per unit time can be computed as follow:

$$I = \frac{1}{T^*} \int_0^{T^*} p' u' dt = \frac{1}{T^*} \int_0^{T^*} \frac{[p']^2}{\rho_\infty c} dt = \frac{p_e^2}{\rho_\infty c} \tag{2.38}$$

It is important to point out that both Equation 2.37 and Equation 2.38 can be applied for every type of plane waves and not only the plane harmonic waves.

2.4.2 Propagation in Ducts

Given that the main topic of this thesis concerns the acoustic performance of a truck silencer it is important to describe how sound waves propagate inside ducts. Nevertheless, before this the concepts of transmission and reflection need to be introduced. In Figure 2.6 it has been reported how a plane wave behaves when it encounters a discontinuity in the medium of propagation. As it can be seen, at the separation between the different mediums, a reflected and transmitted waves are generated. It follows that, for the geometry presented Figure 2.6, an infinite series of waves will emerge from both medium 1 and medium 3. The coefficient R_{ab} represents the ratio between the amplitude of the reflected wave and the incoming wave which is propagating from medium a to b. In [13] it has been shown that it can be computed using the following formula:

$$R_{ab} = \frac{\rho_b c_b \sin(\theta_i) - \rho_a c_a \sin(\theta_t)}{\rho_b c_b \sin(\theta_i) + \rho_a c_a \sin(\theta_t)} \tag{2.39}$$

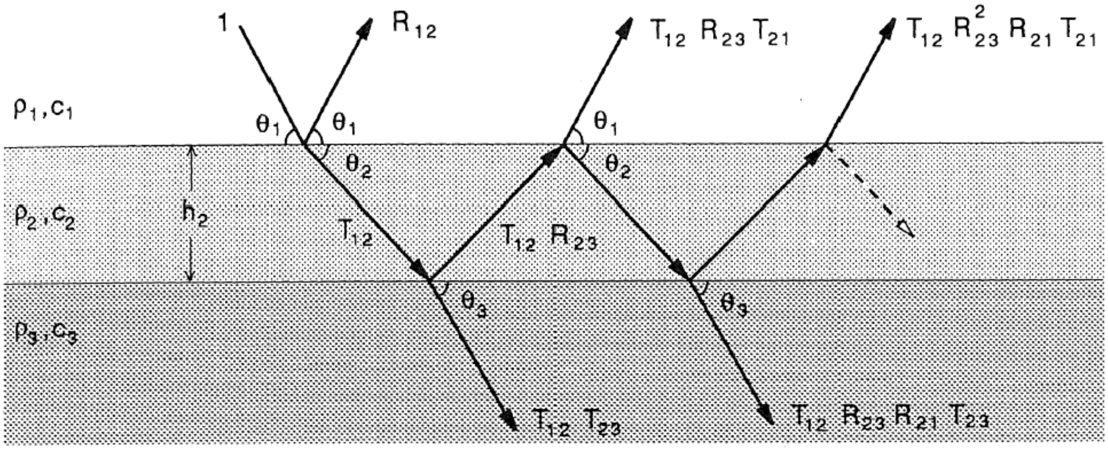

Figure 2.6: Reflection and transmission of a sound ray through a three-layer system of different mediums, [13]

Here θ_i and θ_t are the grazing angle of the incoming and transmitted wave respectively. According to Snell's law these angles are related by the following expression:

$$\frac{\cos\theta_t}{c_b} = \frac{\cos\theta_i}{c_a} \tag{2.40}$$

Similarly, T_{ab} represents the ratio between the amplitude of the transmitted and the incoming wave which is given by:

$$T_{ab} = \frac{2\rho_b c_b \sin(\theta_i)}{\rho_b c_b \sin(\theta_i) + \rho_a c_a \sin(\theta_t)} \tag{2.41}$$

All the coefficients of reflection and transmission visible in Figure 2.6 can be computed using Equation 2.39 and Equation 2.41 if the subscripts are changed accordingly. The same is true also for the angles and Equation 2.40.

If Figure 2.6 is always taken as reference, the total amplitude transmission coefficient T can be obtained from this summation:

$$\begin{gathered} T = T_{12}T_{23}e^{i\phi_2} + T_{12}R_{23}R_{21}T_{23}e^{3i\phi_2} + T_{12}R_{23}^2R_{21}^2T_{23}e^{5i\phi_2} + \\ + T_{12}R_{23}^3R_{21}^3T_{23}e^{7i\phi_2} + \cdots \end{gathered} \tag{2.42}$$

Then, manipulating this expression and making use of the properties of geometric series, Equation 2.42 can be rewritten in this final form:

$$T = \frac{T_{12}T_{23}e^{i\phi_2}}{1 + R_{12}R_{23}e^{2i\phi_2}} \tag{2.43}$$

Here ϕ_2 represents the phase delay between two subsequently transmitted sound rays due to the extra propagation in medium 2 and it can be derived to be equal to:

$$\phi_2 = \frac{\omega h_2}{c_2} \sin\theta_2 \tag{2.44}$$

In Figure 2.7 it has been reported a sketch of a single expansion chamber acoustic filter which can be considered as a very simple model of a muffler. As a matter of fact, abrupt changes in the cross section of a duct are known to reflect part of the wave back to the source leading to a reduction of the overall noise level radiated.

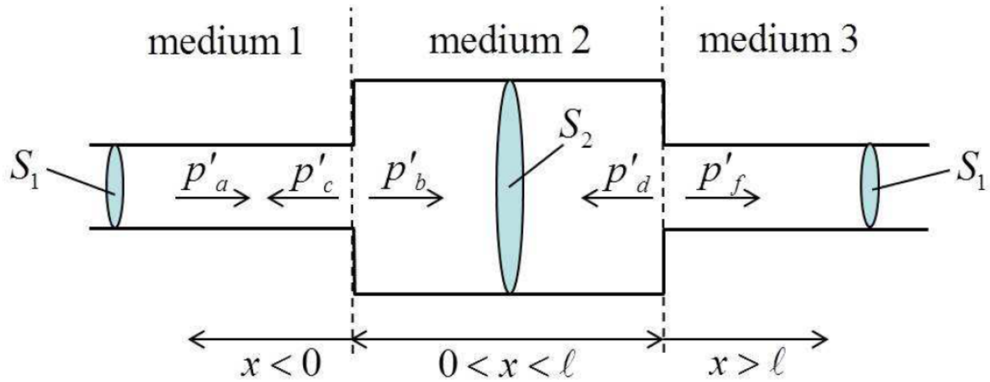

Figure 2.7: Sketch of a single expansion chamber muffler, [13]

Usually, sound waves propagating inside the muffler of a truck have a wavelength that is much larger than the diameter of the duct, hence plane wave propagation can be assumed. As it can be seen from Figure 2.7 the incoming harmonic plane wave $p_a{}'$ is being both reflected and transmitted every time it encounter a discontinuity in the cross section of the duct. Hence this problem can be traced back to a plane wave propagation through a three layer system of different mediums, which have been described previously. From the continuity of both pressure and mass flow at the junctions it can be derived that the reflection and transmission coefficients between the different mediums are given by these expression:

$$R_{12} = \frac{C}{A} = \frac{S_1 - S_2}{S_1 + S_2} \qquad R_{23} = \frac{D}{B} = \frac{S_2 - S_1}{S_1 + S_2} \tag{2.45}$$

$$T_{12} = \frac{B}{A} = \frac{2S_1}{S_1 + S_2} \qquad T_{23} = \frac{F}{B} = \frac{2S_2}{S_1 + S_2} \tag{2.46}$$

where the capital letters represent the amplitude of the respective wave showed in Figure 2.7. After replacing these formulas inside Equation 2.43 it can be found that:

$$\frac{A}{F} = \cos\left(\frac{\omega l}{c}\right) - i\frac{1}{2}\left[\frac{S_2}{S_1} + \frac{S_1}{S_2}\right]\sin\left(\frac{\omega l}{c}\right) \tag{2.47}$$

Then, the transmission loss (TL) can finally be computed as follow:

$$TL = 10\log_{10}\left|\frac{A}{F}\right|^2 = 10\log_{10}\left[1 + \frac{1}{4}\left(\frac{S_1}{S_2} - \frac{S_2}{S_1}\right)^2 \sin^2\left(\frac{\omega l}{c}\right)\right] \tag{2.48}$$

This is a very important parameter that is often used when describing the performance of a silencer. In general the higher the transmission loss the larger will be the noise attenuation. A plot of the transmission loss obtained for this simple case has been reported in Figure 2.8. As it can be seen the transmission loss is maximum for frequencies $f = \frac{c}{4l}, \frac{3c}{4l}, \frac{5c}{4l}, \cdots$ and is equal to zero when $f = 0, \frac{c}{2l}, \frac{2c}{2l}, \frac{3c}{2l}, \cdots$.

It is important to remember that this model is based on the assumption that the wavelength is large if compared to the diameter of the pipe. Therefore, Equation 2.48 lose its validity when frequencies are too high.

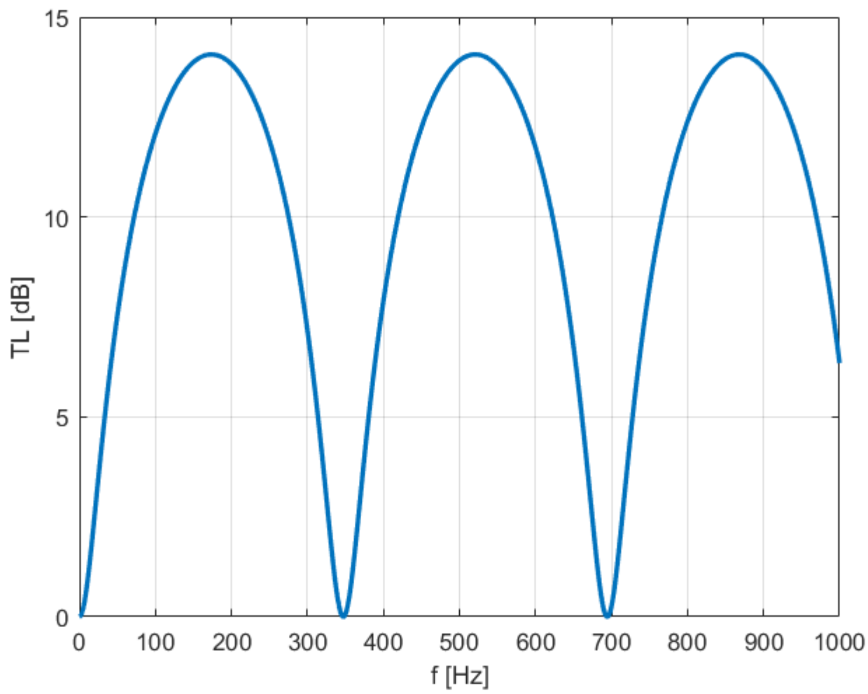

Figure 2.8: Transmission loss plot for the single expansion chamber muffler with $\frac{S_2}{S_1} = 10$ and $l = 0.5$

2.5 Aeroacoustics

Aeroacoustics is a relatively new field of aerodynamics which studies the sound generated by either turbulent flows or aerodynamic forces interacting with surfaces. The origin of this discipline can be traced back to the work of Lighthill [14] who was the first one to introduce the concept of the acoustic analogy. With this approach the flow governing equations are combined such as to obtain one single equation where the wave equation is on the left-hand side and the source terms are all gathered on the right-hand side.

For simplicity, if the fluid is assumed to be inviscid and the source terms are neglected, Equation 2.1 and Equation 2.2 can be simplified as follow:

$$\frac{\partial \rho}{\partial t} + \nabla \cdot (\rho \vec{u}) = 0 \tag{2.49}$$

$$\rho \frac{\partial \vec{u}}{\partial t} + \rho \left(\vec{u} \cdot \nabla \right) \vec{u} + \nabla p = 0 \tag{2.50}$$

Here the equations have been rewritten in vector notation where the symbols ∇ and $\nabla \cdot$ represents the gradient and divergence operator respectively. If Equation 2.49 is multiplied by the velocity and summed to Equation 2.50 it can be found that:

$$\frac{\partial \left(\rho \vec{u} \right)}{\partial t} + \nabla \cdot (\rho \vec{u} \vec{u}) + \nabla p = 0 \tag{2.51}$$

Then, subtracting the divergence of this equation from the time derivative of Equation 2.49 the following relation can be derived:

$$\frac{\partial^2 \rho}{\partial t^2} - \nabla^2 p = \nabla \cdot \left(\nabla \cdot (\rho \vec{u} \vec{u}) \right) \tag{2.52}$$

where $\nabla^2 = \nabla \cdot \nabla$ is the Laplace operator. It follows that if the term $c^2 \nabla^2 \rho$ is subtracted from both side of Equation 2.52 it can be found:

$$\frac{\partial^2 \rho}{\partial t^2} - c^2 \nabla^2 \rho = \nabla \cdot \left(\nabla \cdot (\rho \vec{u} \vec{u}) \right) + \nabla^2 \left(p - c^2 \rho \right) \tag{2.53}$$

which is Lightill's equation. This is an inhomogeneous wave equation where on the right-hand side two source terms can be distinguished. The first one represents the unsteady convection of flow, often known as the Reynolds stress, while the second term is responsible for nonlinear acoustic generation processes. Nevertheless, in many application the second term can be ignored.

In order to derive Equation 2.53 the fluid was assumed to be inviscid. As a matter of fact, in many application the effects of viscosity on the generation of noise can be neglected. Nevertheless, if viscosity were not to be ignored an additional term would appear. In this case Lighthill's equation would be rewritten as follow:

$$\frac{\partial^2 \rho}{\partial t^2} - c^2\nabla^2\rho = \nabla \cdot (\nabla \cdot (\rho\vec{u}\vec{u})) - \nabla \cdot \left(\nabla \cdot \left(\vec{\vec{\Xi}}\right)\right) + \nabla^2 \left(p - c^2\rho\right) \tag{2.54}$$

where $\vec{\vec{\Xi}}$ represents the viscous stress tensor.

The major strength of the acoustic analogy introduced by Lighthill is given by the possibility to separate noise generation from its propagation. As a matter of fact, if the flow noise sources were to be known Lighthill's equation could be used to propagate the noise towards any listener position. Nevertheless, this approach is valid only if the listener is surrounded by quiescent air where the small acoustic perturbations can be accurately described by the homogeneous linear wave equation.

This approach has indeed gained a great popularity in the field of Computational Aeroacoustic (CAA) where first sound sources are resolved in the near-field through numerical simulations and then sound is propagated in the far-field according to the wave equation.

In addition to Lighthill's acoustic analogy, which only consider free turbulent flows, other acoustic analogies have been proposed. Among the most famous there is Curle's analogy [15] which extends Lighthill's analogy by taking into account also hard surfaces and the more general Ffwocs-Williams and Hawkings analogy [16] which is valid for aeroacoustic sorces in relative motion with respect to hard surfaces.

2.6 Signal Analysis

In acoustics it is usually preferable to analyse a sound signal in the frequency domain instead than the time domain. As a matter of fact, by doing so it is possible to:

- identity the dominant noise frequency which could provide insights on the main noise generation mechanism
- correct the noise level by taking into account the sensitivity of human ears at different frequencies

For this purpose the Fourier transform can be used to transform a signal from the time domain to the frequency domain. If $x(t)$ is a time varying signal, like the pressure monitored by a microphone, the continuous Fourier transform is computed as follow:

$$X(f) = \int_{-\infty}^{\infty} x(t)e^{-2\pi ift}\, dt \tag{2.55}$$

where f is the frequency. Similarly the continuous inverse Fourier transform can be used to transform a signal $X(f)$ from the frequency domain into the time domain by performing this integral:

$$x(t) = \int_{-\infty}^{\infty} X(f) e^{2\pi i f t} \, dt \tag{2.56}$$

As it can be seen from both Equation 2.55 and Equation 2.56 ideally an infinite integration time should be considered to perform the Fourier transform and its inverse, but this is not possible in practice. Therefore, the Discrete Fourier Transform (DFT) has to be used instead. Given a discrete time signal x_k, $k = 0, 1, 2, \cdots, N-1$ sampled N times with a time step $\Delta t = 1/f_s$, where f_s is the sampling frequency, the Discrete Fourier Transform and its inverse are computed using Equation 2.57 and Equation 2.58 respectively.

$$X_m = \Delta t \sum_{k=0}^{N-1} x_k e^{-2\pi i t_k f_m} \tag{2.57}$$

$$x_k = \Delta f \sum_{k=0}^{N-1} X_m e^{2\pi i t_k f_m} \tag{2.58}$$

In these equations t_k and f_m are the discrete times and frequencies, k and m goes from 0 to $N-1$ and $\Delta f = f_s/N$.

It is important to note that if a given signal is sampled at a frequency f_s, the maximum frequency that the DFT is able to resolve properly is $f_s/2$ (often referred to as the Nyquist frequency). Frequencies higher than this limit are affected by an error called aliasing and cannot be analysed correctly, [13].

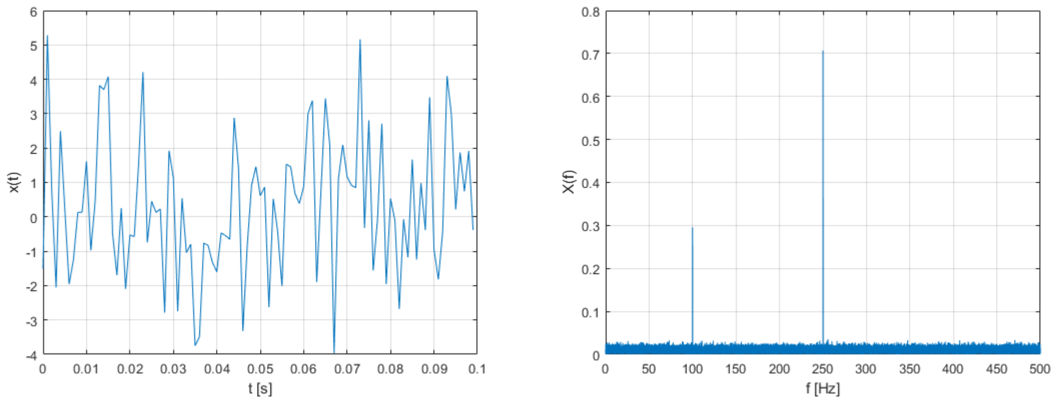

(a) Time signal

(b) Fast Fourier Transform

Figure 2.9: Transformation of a time varying signal in the frequency domain

Several optimized algorithms exists which are able to calculate the DFT quickly. These implementations are thus commonly referred to as Fast Fourier Transforms (FFT). As an example, in Figure 2.9 it has been reported both the time signal and the DFT of a zero mean white noise signal containing a 100 Hz sinusoid of amplitude 0.3 and a 250 Hz sinusoid of amplitude 0.7. It is evident that the two sinusoid can be identified clearly in the frequency domain but not in the time domain. The DFT has been performed using the Matlab FFT algorithm.

Chapter 3

Computational Aeroacoustics

The term computational aeroacoustics, which is often abbreviated as CAA, is generally used to identify any kind of numerical method describing noise radiation from an aeroacoustic source. In this chapter the main numerical methods employed in this field will be first mentioned. Then, further insights will be presented concerning the method that have been used for the development of this thesis. In particular, a series of guidelines and recommendations will be presented on how to properly set-up a CFD simulation with the objective being the analysis of the acoustic characteristics of flows using STAR-CCM+.

3.1 Numerical Methods

All the numerical methods that are generally employed in the field of computational aeroacoustics can be divided in these two main categories:

- **Direct Methods:** This approach consists in resolving both the flow field and the aerodynamically generated acoustic field simultaneously. In other words, the Navier-Stokes equations have to be solved from the noise sources region until the location of the observer. Even if this would be the most accurate method, the biggest disadvantage is related to the high computational cost which is due to the large difference between the flow variables and acoustic variables length scales.

- **Hybrid Methods:** In this case, sound generation and its propagation are treated separately such that the acoustic field can be solved using different equations and numerical techniques from the flow field. Usually, sound sources are computed using CFD simulation methods. Once noise sources are known the sound can be propagated in the far-field using either an analytical method, such as acoustic analogies, or a computational method based on simplified equations. It follows, that the computational time is reduced considerably.

In computational aeroacoustics, for a proper prediction of flow noise, it is of fundamental importance to be able to solve the flow dynamics accurately. For this purpose, computational fluid dynamics (CFD) can be employed. This discipline includes any fluid dynamic problem which is solved with a computer using numerical analysis or algorithms. Nowadays CFD is widely employed by many companies since it allows to analyse different configurations of a given component saving up a lot of time and money if compared to an experimental approach while providing a reasonable level of accuracy. The flow equations can be solved differently depending on many factors such as computational resources or the type of flow which is being analyzed. The three main approaches used in CFD can be gathered as follow:

- **Direct Numerical Simulations (DNS):** The flow governing equations are solved for every length and time scale without introducing any simplifying model. Since the computational power required for this kind of simulations is extremely high, especially for high Reynolds number flows, this approach is not used for industrial applications but rather to study fundamental aspects of flow physics.

- **Large Eddy Simulations (LES):** With this approach only the larger turbulence length and time scales are resolved while the smaller ones are only modelled. As a matter of fact, it has been proven that the larger length scales of a turbulent flow have an anisotropic behaviour, hence they depends strongly on the kind of flow considered, while the smallest scales have a more universal behaviour which can be modelled more easily. The separation between the two scales can be performed using a filtering operation which can be seen as a locally weighted average process over a certain volume of fluid. Since the smallest scales are only modelled the computational time required for a LES simulation is significantly reduced if compared to a DNS simulation. Furthermore, since most of the flow noise is produced by the larger flow structures it can be concluded that this kind of simulations should be able to capture the acoustic characteristic of a flow at a reasonable computational cost. The biggest disadvantage concerns the solution of near wall flows, where the turbulence length scales become very small and the computational power required start to become unsustainable for the industrial world.

- **Reynolds Averaged Navier-Stokes (RANS):** This kind of simulations are the most widely used for industrial application since they are able to provide meaningful results at a low computational price. The main idea is that a turbulent flow can be decomposed in an average and fluctuation component, as described in section 2.2. Then both the flow variables and its equations are averaged. Since the time scale of the average flow motion are much longer if compared to the turbulent motion it can be inferred that the computational time is significantly reduced. Nevertheless, performing this kind of simulations on strongly unsteady or separated flows could be problematic and lead to wrong results. Therefore since sound is an intrinsically unsteady phenomenon it would be preferable to employ LES simulations.

After this short introduction on the available approaches used in CFD it can be concluded that if the objective were to be the analysis of flow generated noise it would be beneficial to have a hybrid method which could combine the computational efficiency of RANS simulation with the accuracy of LES simulations. Based on this idea the Detached Eddy Simulation (DES) method, originally proposed by Spalart and Allmaras [17], has been developed. The name DES has been based on the idea that RANS mode should be employed inside the boundary layer while LES mode should be switch on in the detached region. This way the high computational power required by LES to solve the very small turbulence structures in proximity of a wall is reduced while keeping the higher accuracy offered by LES in the separated region. Despite the initial successes of the original DES model in some applications there was encountered some problems which needed to be taken into account. As a matter of fact, for flows with thick boundary layers or shallow separation it was found an incorrect behaviour due to the switching of the LES mode inside the boundary layer which caused early separation. To solve this problem the Delayed Detached Eddy Simulation (DDES) formulation have been proposed which guaranteed the activation of the LES mode only outside the boundary layer, hence the name.

Nowadays there exist several CFD commercial software such as ANSYS CFX, Fluent or STAR-CCM+ which are all based on different variation of the methods presented in this section. Through the development of this thesis the software STAR-CCM+ has been used to perform CAA simulations. In the next section further insights will be provided on both the software and the guidelines that have been followed to properly set up a CFD simulation with the objective being the analysis of the acoustic characteristics of flows.

3.2 Acoustic Simulations with STAR-CCM+

STAR-CCM+ is a CFD commercial software originally developed by CD-Adapco. In the industrial world STAR-CCM+ is used widely for the simulation of different engineering problem such as fluid flows, electromagnetic, heath transfers and many more. In this work the software has been used mainly to study flow generated noise by performing direct noise calculations. This means that both the noise generating turbulent structures and the radiated sound waves have to be solved from the sound sources until the location of the microphone/probe. The direct noise calculation procedure is the same as when carrying out an unsteady simulation but there are a few important differences that need to be taken into consideration.

First of all, the order of magnitude of the relevant acoustic quantities such as pressure, velocity and density fluctuations can be several order of magnitude lower than the hydrodynamic quantities. This requires the use of a high accuracy solver.

Secondly, since unsteady simulations such as DES/LES are generally computationally expensive it would be beneficial to keep the computational domain as small as possible. Nevertheless, the boundary conditions available in STAR-CCM+ are all partly or fully reflective with the exception of the free stream boundary condition. Therefore, boundary conditions need to be treated with special care such as to avoid spurious reflection from the boundaries.

Thirdly, both the mesh and the time step need to be fine enough such as to be able to resolve both the turbulent flow generating noise structures and the noise radiated from them in the far-field.

These are the three main challenges when performing direct noise calculations using STAR-CCM+. In the following subsections it will be provided a series of guidelines which will address the issues just mentioned. Nevertheless, it is important to point out that the version of STAR-CCM+ that has been used is the following: `Simcenter STAR-CCM+ 2020.1 Build 15.02.007 (linux-x86_64-2.12/gnu7.1-r8 Double Precision)`. If a different version is employed by the reader slight variation to the proposed suggestions could work better.

3.2.1 Mesh Generation

Trimmed meshes are known to provide the least amount of dissipation and high accuracy with less computational cost if compared to polyhedral meshes. Nevertheless, trim meshes are also less suitable for complex geometries. As a matter of fact, a smooth transition in mesh size is difficult to achieve with trim meshes and this could lead to have spurious internal wave reflections. Furthermore, trim meshes often create low quality cells at the transition region between the prism layers and the core mesh. Therefore, since the objective of this thesis is to analyze the acoustic characteristics of a real silencer geometry, polyhedral meshes have been used instead of trim meshes due to their greater adaptability to more complex geometries. Nevertheless, for both type of meshes it is recommended to pick the cell quality remediation model when setting up the physics continuum.

When preparing a mesh for aeroacoustic analysis it is important to ascertain that the mesh will be able to capture both the flow generating noise sources and the propagating waves. Therefore, inside the noise generating region the smallest cell size should be chosen based on the turbulent structures length scales. On the other hand, outside of the sound generating region the cell size should be based on the maximum frequency the simulation is trying to resolve, namely the smallest wave length.

It can be concluded that, before the mesh generation, the highest frequency of interest need to be defined. Once this value is known the size of the mesh in the noise generating region can be decided. One way to check if the chosen mesh size is able to capture the flow generating noise structures is to run first a RANS simulation and then create a mesh frequency cutoff scene of the region where most of the noise is coming from. As a matter of fact, the mesh frequency cutoff value gives an estimate of the maximum frequency the cell size is able to resolve inside the region where the production of flow noise is significant. In case the cell size is found to be either too coarse or too fine the mesh has to be modified accordingly. It is important to note that in order to access the mesh frequency cutoff field function the Aeroacoustics > Broadband Noise Sources with either the Curle or Proudman model have to be selected first.

Regarding the mesh size in the region that goes from the noise sources to the microphones location the best practice is to set the cell length as $\frac{\lambda_{min}}{20}$, where λ_{min} is the wave length of the maximum frequency of interest. This way the propagating waves are generally captured accurately and the numerical dissipation is limited. Furthermore, the grid stretching should be limited to 5% in regions with no flow such as to avoid self reflections. Nevertheless, this limit can be increased by 1% every 10 m/s increase in mean flow velocity.

Another region which is important to consider is the wall. Usually the best practice is to employ a prism layer with a mesh-size growth factor of 1.2 or less. Furthermore, inside strongly separated regions it would be recommended to guarantee a $y^+ < 1$.

Finally, once the mesh has been created, the mesh quality can be checked by using the diagnostic tools offered by STAR-CCM+.

3.2.2 Physics Continuum

The most common models that are usually selected when setting up the physics continuum for direct noise calculation are the following:

- **Implicit Unsteady**
- **Segregated Flow**: Less dissipative and more computationally efficient than the Coupled Flow solver.
- **Ideal Gas**: If the constant density model were to be selected no compressible flow phenomenon, such as sound, could be solved.

- **Segregated Fluid Temperature/Enthalpy**: Since sound is an isentropic process the Segregated Fluid Isothermal option should be avoided because it would lead to an incorrect estimate of the speed of sound.
- **Turbulence**
- **LES/DES**: For wall bounded and high Reynolds number flows it is recommended to use the DES model since LES are known to be more computationally expensive than DES when boundary layer are resolved. Nevertheless, when it is assumed that the fine-scale fluctuations inside the boundary layer would have a great impact on the noise generation the LES model should be chosen instead.
- **Spalart-Allmaras**: This model requires less computational effort if compared to the SST (Menter) K-Omega Detached Eddy model since it solve only for one equation.
- **All y^+ Wall Treatment**
- **Cell Quality Remediation**
- **Gradients**: The Venkatakrishnan gradient limiter should be selected together with the TVB gradient limiting. A field variation factor of 0.2 has been shown to work well [18].

The selection of these models together with the suggested modification to the default settings should guarantee a low numerical dissipation solver which is required when performing aeroacoustic simulations. It is interesting to point out that for direct noise calculations none of the optional Aeroacoustics model available in STAR-CCM+ are actually necessary.

3.2.3 Boundary Conditions

In computational aeroacoustics specifying the boundary conditions takes more care then with conventional CFD simulations. This is because in STAR-CCM+ nearly all boundary types are partly or fully reflective. As a matter of fact, boundary conditions are generally set as constant in time. Therefore when a time varying entity such as a sound wave impinges on the boundary, a reflected wave is generated in order to satisfy the constant boundary condition imposed at the boundary. A solution to this problem would be to employ time varying boundary conditions but this is not always a possibility since the time varying conditions should be known beforehand. It follows that other precautions need to be followed such as to avoid spurious reflections from the boundaries.

The only boundary type available in STAR-CCM+ which has quasi non-reflecting characteristics is the Free Stream boundary. In particular this is true for sound waves that impinges normally on the boundary surface. However, sound waves that impinges at an oblique angle are known to be partly reflected. On the other hand the Pressure Outlet boundary type, which is often used as an outlet boundary condition, is known to be 100% acoustically reflective. Nevertheless, from the 2020.1 release of STAR-CCM+ a non-reflective option is available also for the Pressure Outlet boundary type. If this option is activated the behaviour of the Pressure Outlet boundary, in terms of reflective characteristic, will be similar to the Free Stream boundary.

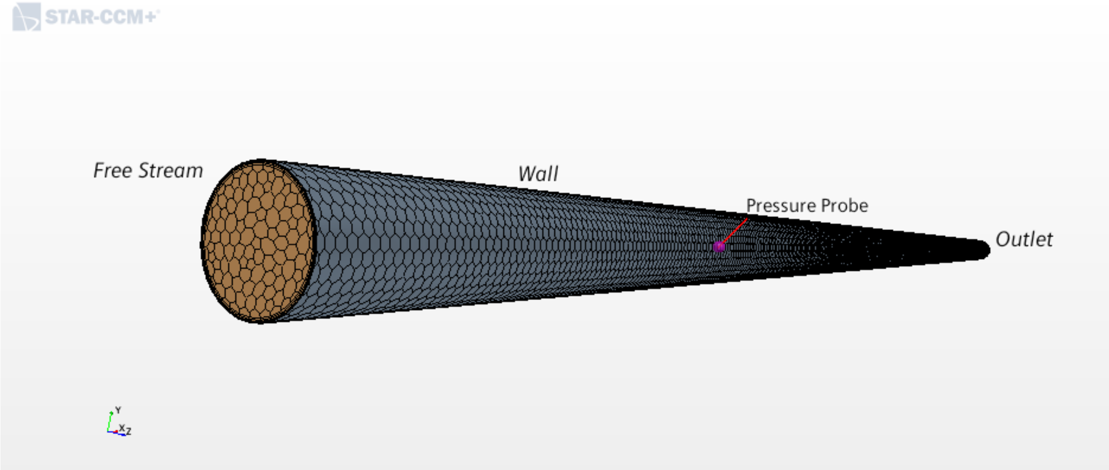

Figure 3.1: Simple straight pipe geometry used to assess the non-reflective characteristics of the outlet boundary

To assess this behaviour a simple straight duct geometry has been created. This can be visualized in Figure 3.1. The inlet boundary condition has been set to Free Stream and a time varying Mach number specified by Equation 3.1 have been imposed.

$$M = Ae^{-[(t-\Delta t)\sigma]^2} \sin 2\pi f(t - \Delta t) \tag{3.1}$$

This generates an acoustic pulse which propagates towards the right of the domain. The variation in time of the signal generated by Equation 3.1 when $A = 0.0001$, $f = 500$, $\sigma = 500$ and $\Delta t = 0.005$ can be seen reported in Figure 3.2. The wall of the pipe has been set as an adiabatic and no-slip wall while the outlet has been changed from Free Stream, with $M = 0$, to Pressure Outlet with either the non-reflective option activated or not. In Figure 3.3 there has been reported the pressure signal monitored by a point probe located 0.5 m away from the inlet boundary. As it can be seen from the comparison both the Free Stream and the non-reflective Pressure Outlet boundary generates small reflection of the incoming acoustic pulse but the Free Stream seems to reflect the least. On the other hand, if the non-reflective option of the Pressure Outlet boundary is not activated the incoming wave is reflected completely.

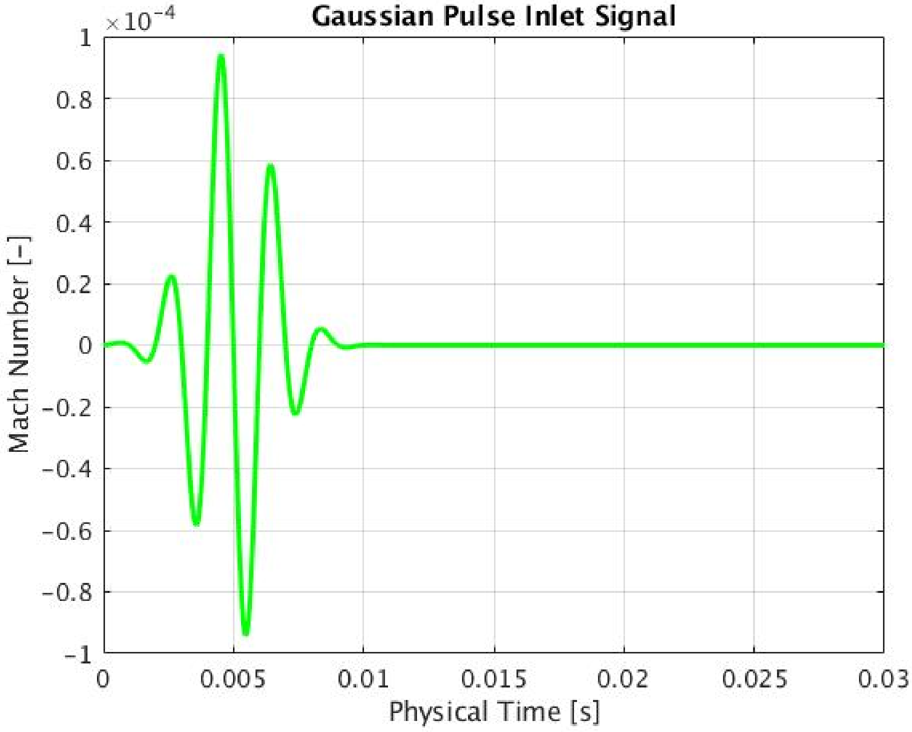

Figure 3.2: Signal of the input Mach Number obtained from Equation 3.1 when $A = 0.0001$, $\Delta t = 0.005$, $\sigma = 500$ and $f = 500$

Even if both the Free Stream and the non-reflective Pressure Outlet boundaries have been shown to be quasi non-reflective a good practice to further reduce the reflective character of those boundaries is to employ them in combination with either an Acoustic Suppression Zone (ASZ) or a stretched grid.

The ASZ can be seen as a sponge zone which aims at absorbing any flow unsteadiness before it reaches the boundary. As a matter of fact, if there were no unsteadiness at the boundaries there would be no reflections as well. The ASZ model has to be selected when setting up the physics continuum. There are three main factors that need to be considered when using an ASZ.

First of all the zone's thickness has to be specified. This is a value that is usually set as 3-5 times the maximum acoustic wavelength of interest.

Secondly, the equations which should include the damping terms have to be decided. It has been proven that activating the ASZ only for the continuity or momentum equations yield an increased robustness. The energy equation damping should not be switched on. Once the equations are selected the proper target that the damped flow variables should reach at the ASZ boundary has to be specified. This can be usually achieved by running a precursor steady state simulation, mapping the obtained solution and specifying those values as the reference values for the Acoustic Suppression Zone boundary.

Thirdly, the ASZ relaxation coefficient must be made vary from zero to its maximum value and this variation has to happen smoothly both in space and time. Generally this can be easily achieved by making a user defined field function with linear or cosine ramping laws for the relaxation coefficient. The maximum value of the relaxation coefficient typically span in the range between hundreds and thousands. It is important to tune this value properly since if the damping is too strong solutions instabilities may occur while if it is too weak the reflection could not be removed well enough.

Another technique that is usually employed in combination with the ASZ is the progressive coarsening of the mesh towards the boundaries. As a matter of fact if the grid size is large enough both the acoustic waves and the flow unsteady structures will be damped through numerical dissipation since the mesh is not able to resolve those entities. Due to the rapid increase in mesh coarsening the number of additional cells is not so large such as to increase the computational time considerably. Nevertheless, if the stretching factor between two consecutive cells is too aggressive, it has been found that self-reflections may occur [18]. Therefore, to avoid this problematic a stretching factor lower than 5% is recommended especially in regions with low mean flow. As a matter of fact, when the mean flow velocity is increased it has been found a reduced amount of self reflections which allow to increase the stretching factor. For convenience, in Appendix A it has been reported the Matlab code that has been used to calculate the stretching factor of a mesh region obtained through extrusion in STAR-CCM+ when thickness, number of layers and initial wall thickness are specified by the user. This code could be used to check if the stretching factor is either too aggressive or not.

It is worth noting that both the ASZ and the stretched grid can be applied to any boundary type in order to dissipate the unsteady flow structures before they reach the boundary. Nevertheless, it can be concluded that in the regions where these treatments are applied the solution will be non-physical. It follows that all the microphones and visualization scenes should be placed outside of these regions.

3.2.4 Solution Initialization with RANS

For all transient simulations, convergence can be achieved faster if a steady-state RANS simulation is run first and employed for initialization of the transient run.

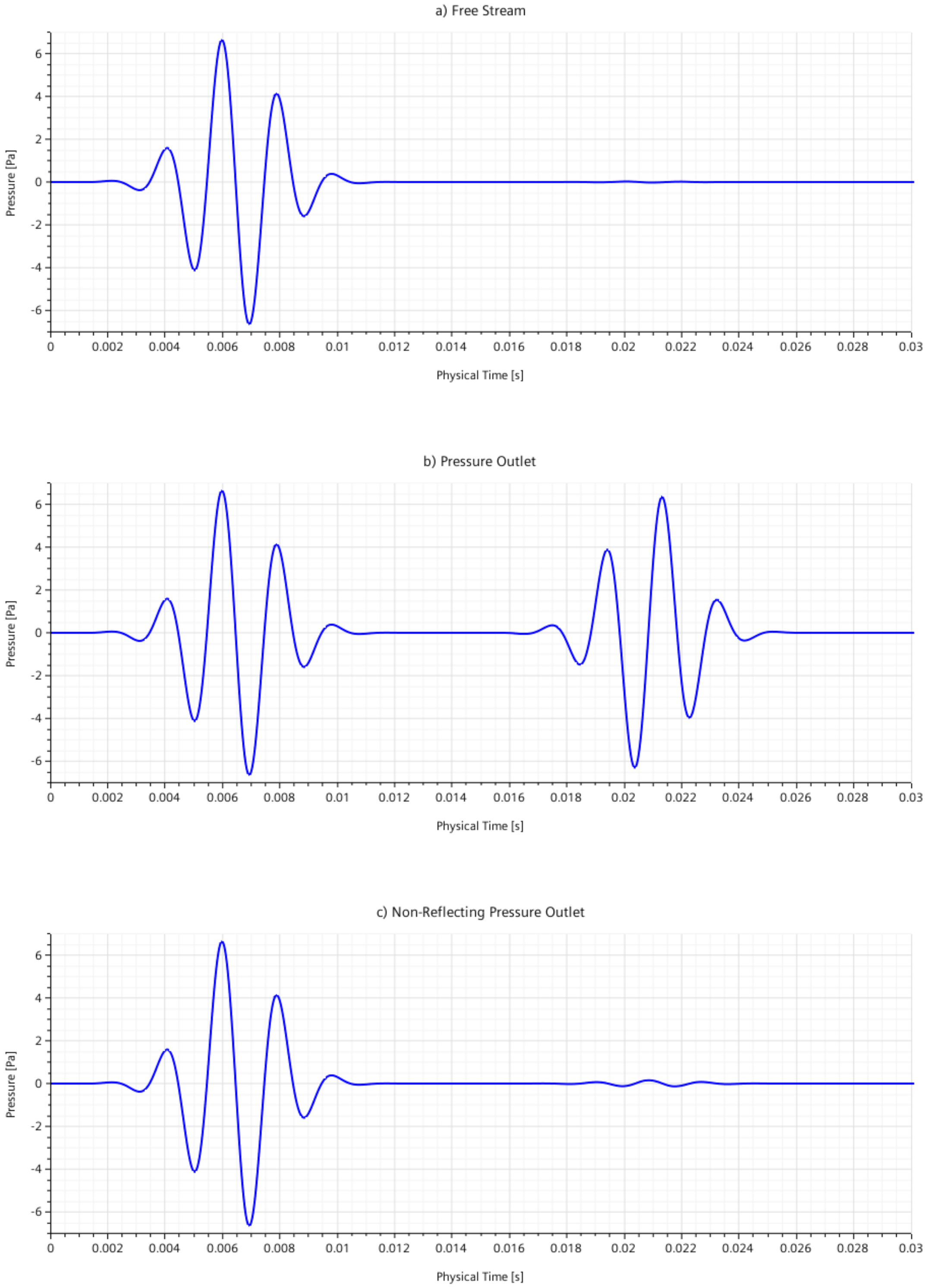

Figure 3.3: Effect of the outlet boundary on the reflection of the monitored pressure signal

If the Segregated Flow model have been selected for the physics continuum the Continuity Initialization option is advised to be activated from the solver settings. This procedure initialize the flow field by solving the continuity equation and it has to be used for the steady-state simulation only.

When performing the precursor RANS simulation it could be useful to employ the Broadband Noise Source models as a tool for qualifying the volume mesh before the transient acoustic analysis. These models can be selected when setting up the physics continuum by activating the models reported in Table 3.1.

Group Box	**Model**
Optional Models	Aeroacoustics
Aeroacoustics	Broadband Noise Sources
Broadband Noise Source Models	Noise Source Models
Noise Source Models	Curle Proudman

Table 3.1: Broadband Noise Source models available in STAR-CCM+ for the precursor RANS simulation.

Once these two Noise Source Models are activated two additional field functions will appear. Namely the Curle Surface Acoustic Power and the Proudman Acoustic Power. The first one compute the sound generated from dipole source terms, hence the sound emitted from the fluctuating surface pressure with which the solid boundary acts on the flow. The second one compute the sound radiated from quadruple source terms, hence the acoustic power emitted from the turbulent flow structures. Therefore, if plotted on a scene, these two field functions can give an idea on where are located the main flow generating noise sources. Once the source region are identified the Mesh Frequency Cutoff field function can be plotted in the same location. As a matter of fact, this field function becomes available when either the Curle or the Proudman model are activated. This gives an estimate on the maximum frequency the current mesh is able to resolve. If it is found that in the region where most of the flow noise sources are located the Mesh Frequency Cutoff is lower than the maximum frequency of interest a mesh refinement should be applied. This process should be repeated until the Mesh Frequency Cutoff is equal or higher than the desired maximum frequency of interest.

3.2.5 Solver Settings for the Transient Simulation

The choice of the time-step for the Implicit Unsteady solver usually is based on the maximum frequency the simulation is trying to resolve. The best practice is to choose a time-step which is smaller than one twentieth of the time period associated to the maximum frequency of interest, hence $\delta t < \frac{1}{20 f_{max}}$. In addition the temporal discretization should be set to 2nd-order.

Regarding the Segregated Flow solver both the velocity and pressure under-relaxation factors are recommended to be set as high as possible such as to increase the convergence speed while maintaining solver robustness. Generally these under-relaxation factors are initially set with a robust starting value but then they are increased gradually while monitoring the convergence per time-step. Good starting values for the velocity and pressure under-relaxation factors are 0.8 and 0.5 respectively. On a good quality mesh it should be possible to increase these values safely until 0.9.

Enabling the High-Accuracy Temporal Discretization option for both the Segregated Flow and Segregated Energy solver is always beneficial since it can significantly increase the simulation accuracy without affecting the computational effort drastically. The Optimized 2nd-order (5) option is recommended.

3.2.6 Stopping Criteria

For the precursor steady-state RANS simulation convergence can be considered fully achieved when all the monitored residuals adopt an oscillatory pattern about a mean value. The Maximum Steps should be chosen sufficiently high such that the simulation is able to reach full convergence. Nevertheless, if the steady-state approach does not satisfy the real physics of the problem convergence can not be fully achieved. An unsteady approach should be followed instead. However, even if not fully converged the precursor steady-state simulation can always be employed to evaluate the mesh quality before running the more computational expensive transient simulation.

When performing the transient simulation the Maximum Steps stopping criteria should be disabled. The Maximum Inner Iterations and the Maximum Physical Time should be enabled instead. The Maximum Inner Iterations stopping criteria controls the number of iterations that are carried out within a physical time-step. Generally, this stopping criteria can be chosen following a trial and error procedure. For this purpose a point probe that evaluate a flow variable of interest, such as pressure or velocity, need to be created using Maximum Report. Then a monitor and plot can be associated to the Maximum Report created. It is important to ensure that the monitor trigger is set to Iteration rather than Time Step. If the monitored quantity is able to reach an asymptotic value within the maximum number of inner iterations specified it means that increasing the number of inner iteration would not change the results. On the other hand the computational time could be reduced if the number of inner iteration is reduced. Nevertheless, it should be ascertained that the monitored quantities are able to reach the asymptotic behaviour within the maximum number of inner iterations specified. In [18] it has been suggested to use a number of Maximum Inner Iterations around 4-5. If convergence is found to be a problem the time-step can always be reduced. As a matter of fact, the smaller the time-step the smaller would be the changing of the solution from one step to the next.

Finally the Maximum Physical Time has to be chosen. This is a case-dependent parameter and it has to be set long enough such as to flush out all the transient startup artifact until the flow is stabilized. At the same time it has to guarantee that a sufficiently long sampling time has been considered for the post-processing of the results. Typically the rule of thumb is to estimate this stopping criteria as the time it takes the flow to travel through the computational domain a couple of times. Once the simulation is concluded, if it seems that the simulation would have yielded more accurate results if the Maximum Physical Time were chosen higher, its value can always be increased and the simulation can be continued to run until the desired physical time has been reached. It is worth noting that properly resolving low frequency phenomena generally require a higher Maximum Physical Time if compared to high frequency phenomena.

3.2.7 SPL Calculation

The computation of the Sound Pressure Level of all the pressure signals monitored during the simulation can be obtained easily in STAR-CCM+. As a matter of fact it is simply required to create a New Point Time Fourier Transform from the Tools > Data Set Functions node and specify the desired properties. For the SPL calculation Sound Pressure Level has to be selected as the Amplitude Function. The Analysis Blocks are by default set to 1. This means that the full signal is accounted for in the computation of the FFT. If the number of anaylsis block is increased to $N > 1$, the signal is subdivided into N parts of equal time length, the FFT is computed for each signal fragments and the final FFT is obtained through an averaging process. By increasing the number of Analysis Blocks a smoother spectrum can be obtained but the frequency resolution will be decreased since the number of samples of the signals associated to each block is lower if compared to the full signal. However, the number of the Analysis Blocks can also be increased without reducing the length of the associated signal fragments. This can be obtained by using an Overlap Factor different than zero, which is usually recommended. The important thing is to always compare SPL with the same frequency resolution, otherwise the comparison would be meaningless.

Another important property that is usually advised to switch on is the Window Function. These functions are used to modify the signal such as to reduce the error made by the FFT algorithm due to the assumption of a periodic input signal.

Regarding the Start Time and the Cut-off Time they have to be selected such that all the initial transient startup artifacts are not included in the signal and the sampling time is long enough to yield accurate SPL frequency resolution.

In STAR-CCM+ there is also the possibility to compute the A, B or C-weighted SPL directly if they are selected as the Amplitude Function. These weighted sound pressure levels are useful when the loudness of sound need to be taken into consideration. As a matter of fact, since human ears are sensitive to the frequency the noise is perceived, two SPL of equal amplitude could be perceived as differently loud if the frequency is not the same. A-weighting is the most commonly used in the regulations for industrial noise. In Equation 3.2 it has been reported the functional form of the A-weighting curve as a function of frequency.

$$A(f) = \frac{12200^2 f^4}{(f^2 + 20.6^2)(f^2 + 12200^2)\sqrt{(f^2 + 107.7^2)(f^2 + 737.9^2)}} \tag{3.2}$$

Then, the corresponding gain function R_A is computed as follow:

$$R_A(f) = 2 + 20\log_{10}(A(f)) \tag{3.3}$$

Finally the A-weighted SPL is derived by summing the gain function (which could also be negative) to the actual SPL.

3.2.8 Simulation Methodology Summary

In this section it will be presented a brief description of the simulation methodology employed to perform direct noise calculations in STAR-CCM+. In Figure 3.4 it can be seen a flow chart which summarizes the main steps.

The first thing to be done is to define the computational domain. For this purpose, the software ANSA were used for the generation of the surface mesh which later was imported in STAR-CCM+. Here the Volume Mesh was generated after all the desired mesh characteristics were specified.

Once the computational domain has been defined, it has to be decided if for the problem at hand the precursor RANS simulation is either required or not. Usually when the problem analysed involves a flow the precursor steady simulation is always recommended for the initialization of the unsteady simulation and to check the mesh quality. An exception is the case when only sound propagation in a quiescent fluid is being simulated. If it is the case to run the precursor RANS simulation then the physics continuum and the boundary conditions have to be set according to the specific problem at hand. Once the RANS simulation has finished to run it is always better to plot the Mesh Frequency Cutoff in a scene where most of the noise sources are located. This allow to qualitatively understand if the mesh generated is fine enough to capture the turbulent-flow noise-generating structures until the maximum frequency of interest.

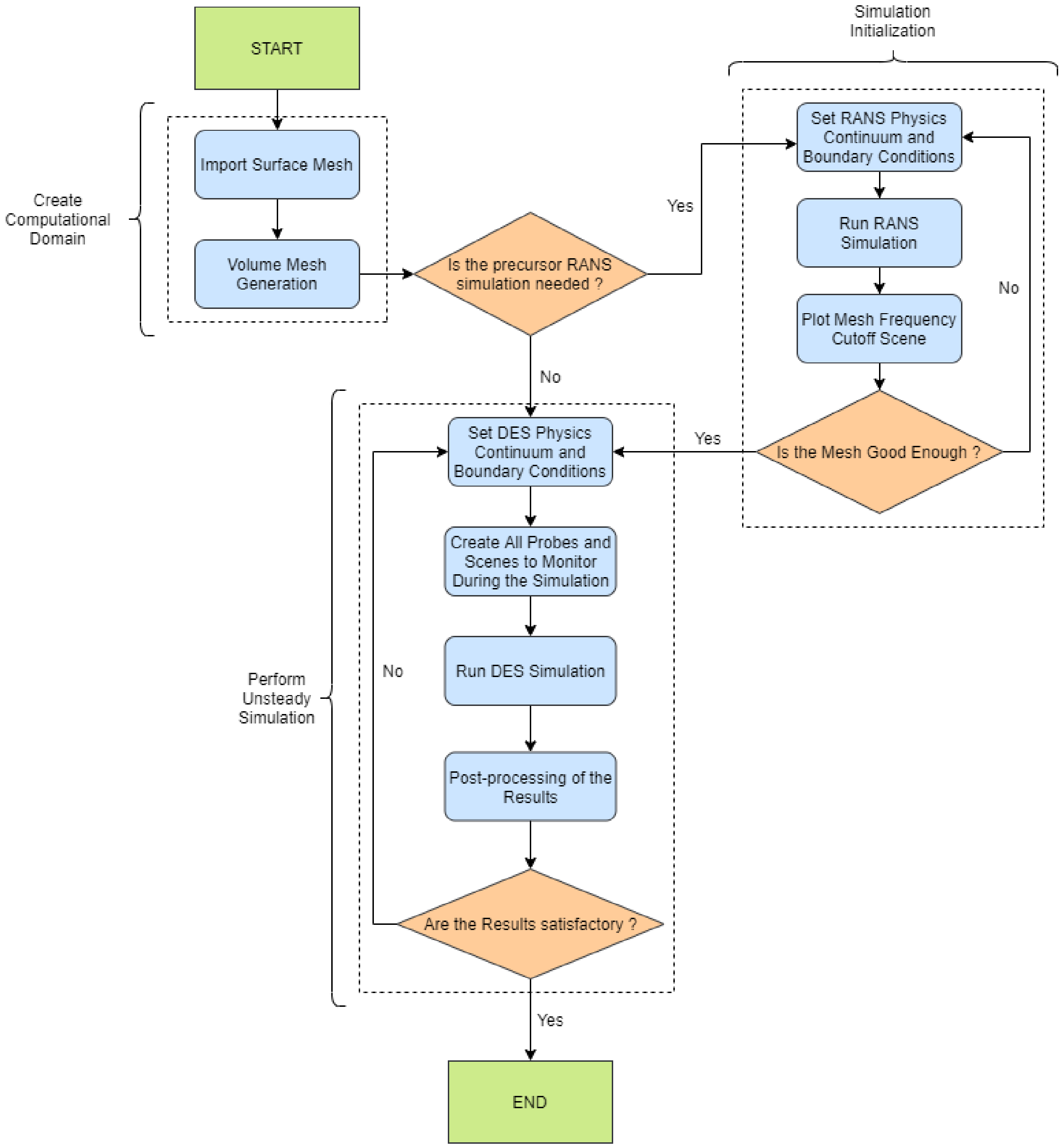

Figure 3.4: Flow chart of the simulation methodology employed to perform direct noise calculations in STAR-CCM+

On the results obtained from the steady state simulation the DES simulation can be initialized. Also in this case the physics continuum have to be defined and the boundary conditions have to be adjusted such as to guarantee non-reflective boundaries. Before running the DES simulation all the probes and scenes which need to be monitored during the simulation have to be set. Finished also this step the transient simulation can be started. Once it has concluded to run the results can be post-processed either directly in STAR-CCM+ or by exporting them in another software like Matlab. Finally if the obtained results are satisfactory, the simulation can be considered concluded. Otherwise the simulation have to be started again making the appropriate adjustments.

Chapter 4

Method Validation

Before implementing the recommendations presented in the previous chapter directly on a complex and expensive CFD simulation it would be better to validate the method developed first. As a matter of fact, if the method validity were not to be proved a significant amount of time could be wasted on a complex simulation that eventually would yield only to wrong conclusions. For this purpose, the results of two experiments found in open literature have been used.

The first benchmark case involve the validation of a CFD simulation with experimental data obtained from simple silencer configurations. In particular the transmission loss (TL) of a single expansion chamber and an expansion chamber with a baffle will be computed. The calculation of the TL has been achieved through the implementation of the decomposition method. For completeness a brief description of this method will be included in this chapter as well. The CFD set up has been obtained following the guidelines reported in the previous chapter. Nevertheless, with this benchmark case only the STAR-CCM+ solver's ability to capture acoustic phenomena will be tested since the flow effects have been completely ignored.

The second case concerns the simulation of a flow through a duct with a plate. This is an experiment that has been specifically designed for the validation of unsteady CFD simulations and CAA calculations withing an HVAC (Heating, Ventilation and Air Conditioning) system. Since the main objective of this thesis concerns the development of CFD simulation methods to resolve acoustic characteristic of flows this is a particularly interesting validation case. As a matter of fact a lot of flow-generated noise is caused by obstacles inside air ducts. These flow obstructions are known to cause unsteady flow motions such as separations which increase both the noise and turbulence level.

Overall, through this chapter it will be shown that the results obtained with STAR-CCM+ agree well with both benchmark cases. Therefore, the developed method is ready to be tested on more complex geometries.

4.1 Simple Muffler Configurations

In this section the ability of the guidelines reported in the previous chapter to capture acoustic phenomena will be tested by comparing CFD simulations with experimental results published in [19]. In particular, the experiments relate to the measurement of the Transmission Loss (TL) of two simple silencer configurations, namely a single expansion chamber and an expansion chamber with a baffle. In Figure 4.1 the geometries of the two simulated silencers have been reported and the location of the microphone that will be used for the monitor of the propagating sound waves have been highlighted. The dimensions of the two silencers analysed have been gathered in Table 4.1.

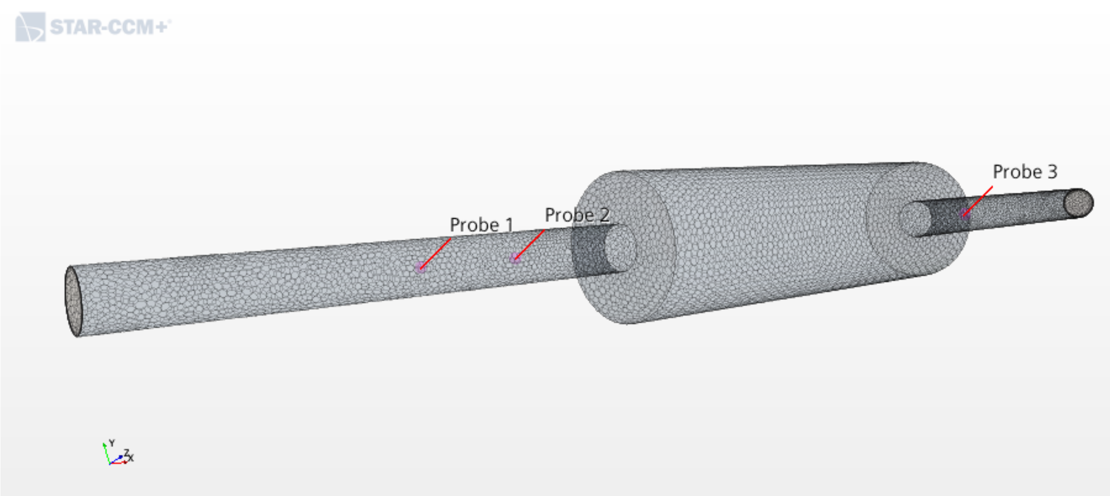

(a) Single expansion chamber

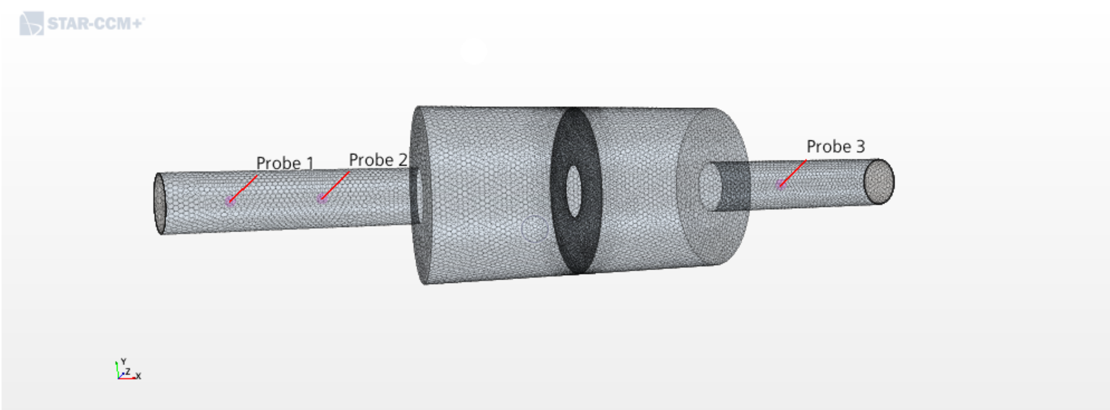

(b) Expansion chamber with baffle

Figure 4.1: Geometries of the simple silencer configurations simulated

Single Expansion Chamber	
Pipe Diameter	48.59 mm
Expansion Chamber Diameter	153.18 mm
Expansion Chamber Length	540 mm
Expansion Chamber with Baffle	
Pipe Diameter	48.6 mm
Expansion Chamber Diameter	153.2 mm
Expansion Chamber Length	280 mm
Baffle Orifice Diameter	48.6 mm

Table 4.1: Dimensions of the simple mufflers configurations, [19]

For the simulation set up the Free Stream boundary condition has been used both at the inlet and outlet boundary of the pipe such as to avoid any reflection of the impinging sound waves. All the other surfaces have been defined as walls. At the inlet boundary a broadband noise source whose frequency range span from 500 Hz to 1500 Hz has been simulated. For this purpose the Mach number of the inlet Free Stream boundary has been defined as in Equation 4.1, where $A = 10^{-5}$ and ϕ_n is a random phase shift. The spacing between the discrete frequencies f_n has been imposed equal to 5 Hz.

$$M = A \sum_{n=1}^{N_f} \sin\left[2\pi\left(f_n t + \phi_n\right)\right] \tag{4.1}$$

In order to specify this time-varying Mach number at the inlet boundary, first Equation 4.1 has been implemented in Matlab and evaluated in time steps of $2.5 \cdot 10^{-5}$ s from 0 to 0.4 s. Then the Matlab generated signal has been imported in STAR-CCM+ as a time-varying table which can be associated to the inlet boundary easily. Since both the time step and the time period used for the simulation are the same that were used for the generation of the time-varying Mach number in Matlab, interpolating the signal has been avoided. The average value of the inlet Mach number and the value specified at the outlet boundary are both equal to zero since no flow have been considered for these simulations. It follows that the precursor steady-state simulation is not required because it is sufficient to initialize the solution as still air.

Regarding the selection of the models for the Physics Continuum, which is visible in Figure 4.2, the guidelines of the previous chapter have been followed. The only default setting that has been changed concerns the Gradients model for which the TVB Gradient Limiting has been activated and the Acceptable Field Variation Factor has been imposed equal to 0.2.

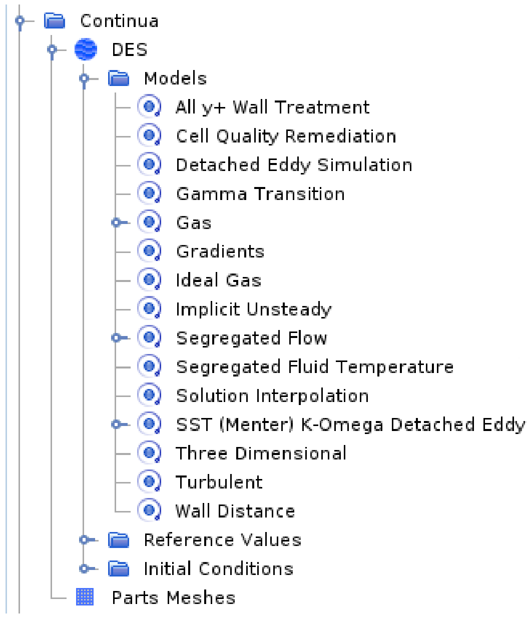

Figure 4.2: Physics Continuum

The transmission loss of both silencer configurations have been calculated following the decomposition method. The silencer TL is usually defined as the ratio between the incident and transmitted acoustic power:

$$TL = 10 \log_{10} \left(\frac{W_i}{W_t} \right) \tag{4.2}$$

The transmitted sound power can be easily obtained by measuring the sound pressure with a microphone placed downstream of the silencer. As a matter of fact, assuming plane wave propagation and an anechoic termination (no wave reflection), the transmitted sound power can be related to the effective sound pressure directly through this expression:

$$W_t = \frac{{p_t}^2}{\rho c} S_o \tag{4.3}$$

where S_o is the area of the outlet pipe. However, since the propagating wave is reflected back when it encounters the muffler, the incident sound pressure is not so easy to be measured. Nevertheless, the inlet wave can be decomposed into its incident and reflected component using the pressure signal monitored by two microphones placed upstream of the silencer.

In Figure 4.3 it has been reported a sketch of the set up required for the calculation of the transmission loss using the decomposition method. As it was shown in Figure 4.1 the set up used in the simulation was similar. The Free Stream boundary condition imposed at the outlet boundary simulate the behaviour of an anechoic termination quite well and the speaker is simulated by the time varying Mach number imposed at the inlet boundary.

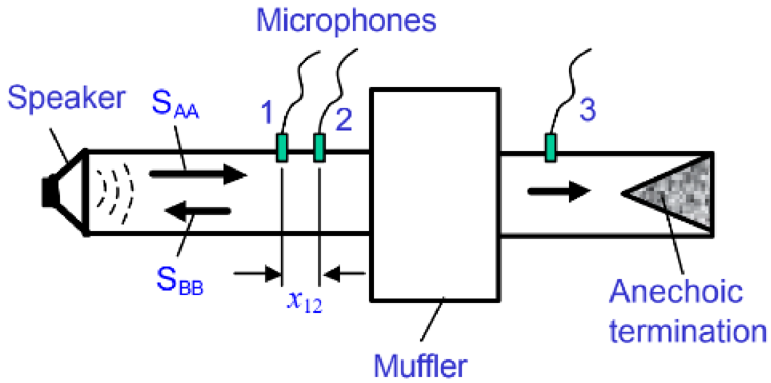

Figure 4.3: Decomposition method reference set up, [20]

According to [21] the auto spectrum of the incident sound wave S_{AA} is:

$$S_{AA} = \frac{S_{11} + S_{22} - 2C_{12}\cos kx_{12} + 2Q_{12}\sin kx_{12}}{4\sin^2 kx_{12}} \tag{4.4}$$

where S_{11} and S_{22} are the auto spectra of the total acoustic pressure measured at microphones 1 and 2 respectively; C_{12} and Q_{12} are the real and imaginary parts of the cross spectrum between the total acoustic pressured measured at point 1 and 2; k is the wave number and x_{12} is the distance between the two microphones. The effective sound pressure of the incident sound wave p_i is related to its auto spectrum by the following equation:

$$p_i = \sqrt{S_{AA}} \tag{4.5}$$

Once this quantity is known the incident sound power can be simply computed using this relation:

$$W_i = \frac{{p_i}^2}{\rho c} S_i \tag{4.6}$$

where S_i is the cross sectional area of the inlet pipe. Substituting Equation 4.3 and Equation 4.6 inside Equation 4.2 the transmission loss can finally be written as follow:

$$TL = 20\log_{10}\left(\frac{p_i}{p_t}\right) + 10\log_{10}\left(\frac{S_i}{S_o}\right) \tag{4.7}$$

It can be noticed that if the cross section of the inlet and outlet pipe are equal the second term can be ignored.

Regarding the solver setting used for the simulation the recommendation given in the previous chapter have been followed, see subsection 3.2.5. Therefore the Segregated Flow under-relaxation factor of the velocity and pressure have been increased to 0.9 and 0.7 respectively and the high-accuracy temporal discretization have been enabled and set to optimized 2nd-order (5).

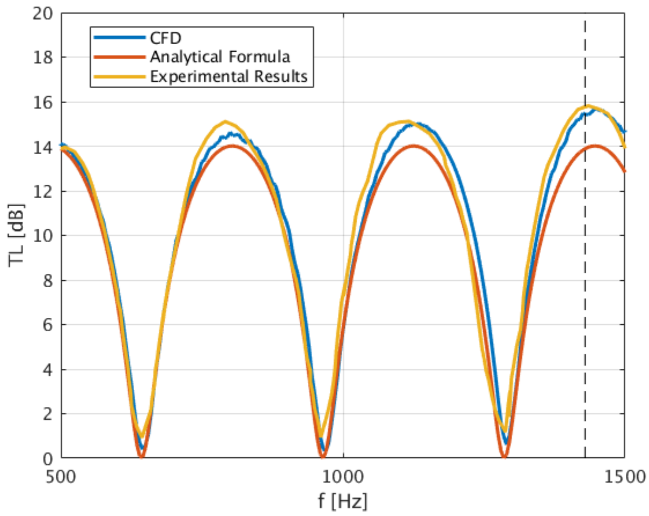

(a) Single expansion chamber

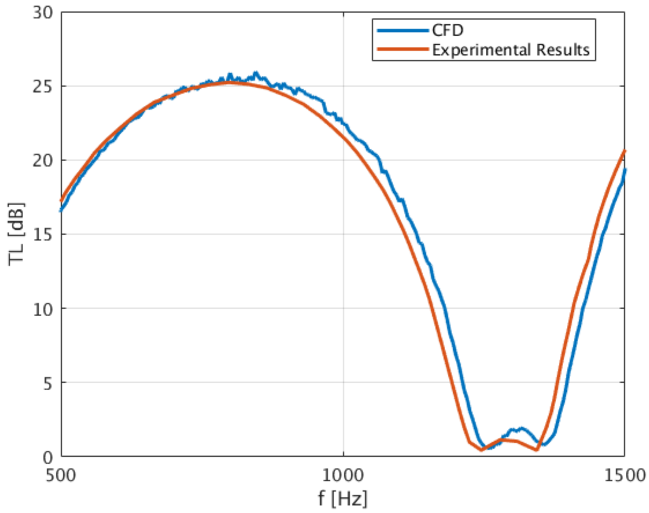

(b) Expansion chamber with baffle

Figure 4.4: TL plots comparison

Once the simulation have finished to run, the pressure signal monitored by the three microphones have been exported in Matlab. The TL has been computed following the decomposition method and then plotted together with the experimental results to ease the comparison. The results obtained for both silencer configurations have been reported in Figure 4.4. In Figure 4.4a it has been plotted also the TL as given by the analytical formula defined by Equation 2.48. This analytical formula usually is considered valid only if the wavelength is larger than five times the diameter of the pipe. This limit is identified by the black dashed line in the same picture and for frequencies above this value the model that underlies the analytical expression loose its validity. Nevertheless, overall it can be concluded that the TL agree very well with the experimental results for both the single expansion chamber and the expansion chamber with the baffle. Therefore it has been proved that applying the guidelines reported in the previous chapter yield accurate acoustic results as long as no flow effects are considered.

In Appendix B the Matlab code that has been used for the generation of the noise signal to be applied at the inlet Free Stream boundary together with the code used for the computation of the TL has been reported.

4.2 Simple HVAC System

The second benchmark case that has been used for the validation of the simulation methodology relate to an experiment carried out by a consortium of the German car manufacturer Audi, BMW, Daimler, Porsche and Volkswagen on the feasibility of predicting the aerodynamically generated noise within an HVAC (Heating, Ventilation and Air Conditioning) system with CFD [22]. The experiment has been specifically designed to validate unsteady CFD simulations concerning noise generated by flaps or other obstacles inside an air conditioning system. As a matter of fact, flow obstructions within air ducts and vents are known to cause flow separation and increase the level of turbulence which eventually can lead to an increase in both broadband and tonal noise. It follows that an accurate prediction of flow generated noise through numerical methods would be a major improvement for the design of silent HVAC systems, especially during the early design stage when hardware is yet not available for experiments.

The experiment has been performed on a radically simplified representation of an HVAC system which include the main flow characteristics of a real HVAC system, namely pressure driven flow separation and flow around an obstacle. The geometry, reported in Figure 4.5, is made of a rectangular duct with a 90° bend and a 30° deflected flap inserted close to the outlet section.

Within the experiment an average flow speed of 7.5 m/s was applied at the inlet of the duct. Precautions were taken concerning the cancellation of the background noise generated by others experimental components. An additional 3 m length of duct was attached at the inlet such as to ensure a fully developed turbulent flow.

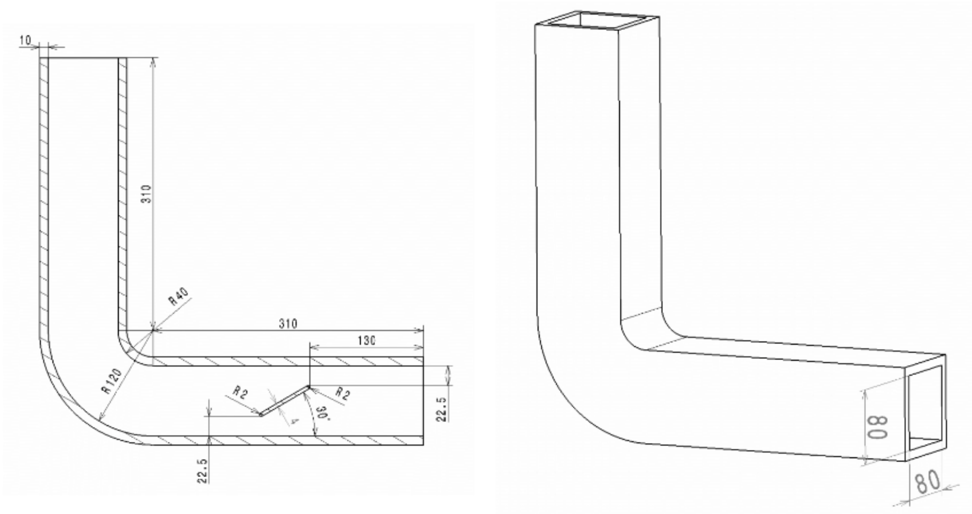

Figure 4.5: Simple HVAC system geometry (all dimensions are expressed in millimeters), [22]

Unsteady wall pressure fluctuations were measured at 7 different locations within the duct by mean of wall flush mounted 1/4 inch microphones. The position where the microphones are placed inside the duct has been reported in Figure 4.6.

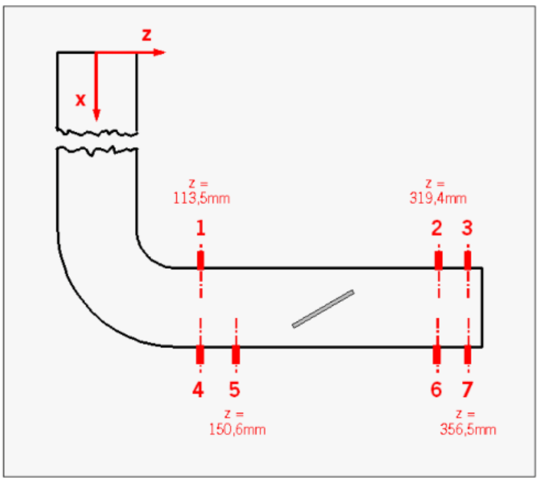

Figure 4.6: Location of the 7 flush mounted microphones used to measure the unsteady wall pressure fluctuations, [22]

The average flow field has been measured using Particle Image Velocimetry (PIV). This experimental technique is based on seeding the flow with reflective particles which are illuminated by two consecutive laser pulses. The reflected light is captured by a camera that generates one picture for each of the laser pulse. Two pictures are thus obtained which gives the position of the particles at two different time instants. Knowing the time step which separates the pulses and by performing cross correlation between the two images the flow velocity field can be reconstructed. Then if the results obtained from many different couples of laser pulses are averaged the average flow field can be determined. In Figure 4.7 it has been reported the experimental set up used for the PIV part of the experiment. Here it can be seen that an acrylic duct has been used for the duct since it is transparent to light.

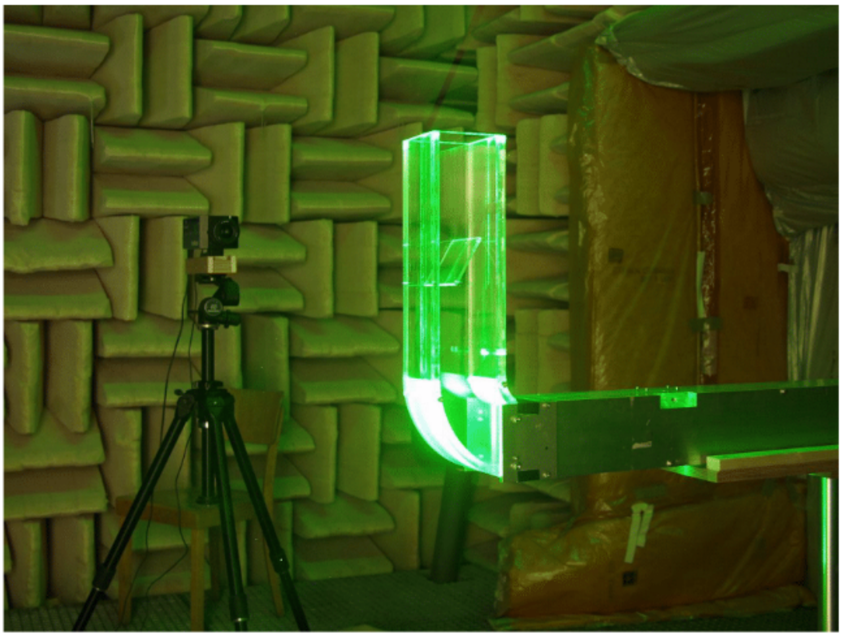

Figure 4.7: PIV measurement set up, [22]

The same experiment have been simulated in STAR-CCM+ with the objective being the validation of the simulation method that will be used on the real silencer geometry. The computational domain have been generated using ANSA and the geometry has been imported in STAR-CCM+ as a surface mesh. In Figure 4.8 it has been reported the outline of the computational domain projected on a plane section. All the geometry dimensions that are not specified in Figure 4.8 have been defined according to Figure 4.5 and a 3 m long pipe have been added at the inlet such as to guarantee a fully developed turbulent flow before it reaches the 90° bend.

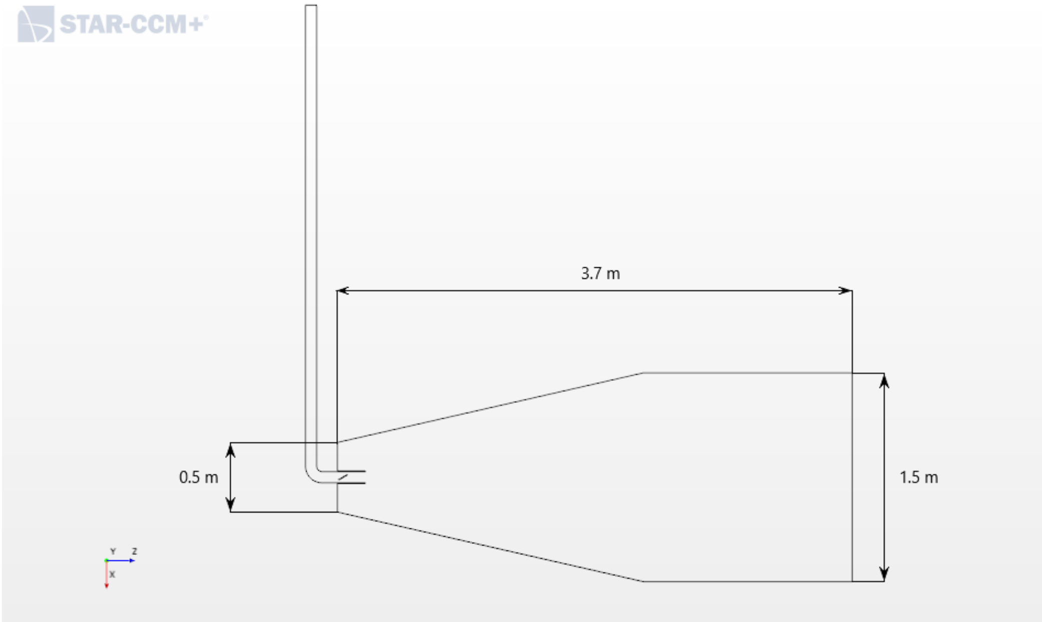

Figure 4.8: Outline of the computational domain used for the simulation of the simple HVAC system

Regarding the mesh, a polyhedral mesher has been used with a fine mesh size of 2.5 mm in the region where both the bend and the flap are located, see Figure 4.9a. This ensured that the turbulent structures were solved accurately in the region where most of the flow unsteadiness were being generated. The furthest section of the cone surrounding the exit of the pipe has been extruded 1.5 m in order to coarsen the mesh such as to numerically dissipate the flow unsteadiness before it reached the boundary. To avoid self reflection of the sound waves due to an excessive stretching of the cells inside the extruded mesh the code reported in Appendix A has been used. Using 40 layers and an initial wall thickness of 10 mm a stretching factor of 5.88% has been obtained, which according to [18] should be small enough to avoid this problematic. In Figure 4.9b a close up view of the extruded and stretched grid has been reported.

Concerning the near wall mesh a prism layer have been applied. Using a 1.5 mm layer thickness close to the flap and a 3 mm thickness everywhere else, both with 10 layers and 1.2 stretching, a wall $y+$ lower than 5 was obtained. Nevertheless, since the All $y+$ Wall Treatment model were selected for the Physics Continuum the strict requirement of $y+ < 1$ does not necessarily need to be satisfied. As a matter of fact the All $y+$ Wall Treatment model employs blended wall functions that emulate Low $y+$ Wall Treatment for fine meshes and the High $y+$ Wall Treatment for coarse meshes. Therefore a reasonable level of accuracy can still be obtained also on meshes of intermediate size. Furthermore, since for the case analyzed most of the flow noise is assumed to be generated from the turbulent structures far from the boundary layer, using a Low y+ Wall Treatment would only increase the computational time without actually yielding a more accurate acoustic prediction.

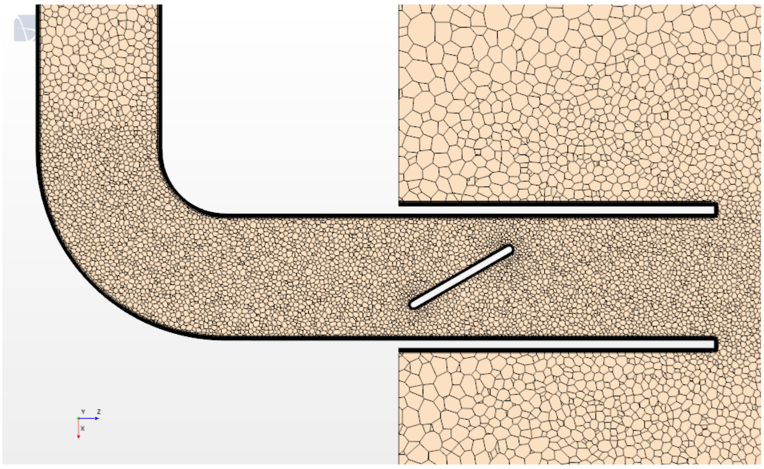

(a) Fine mesh

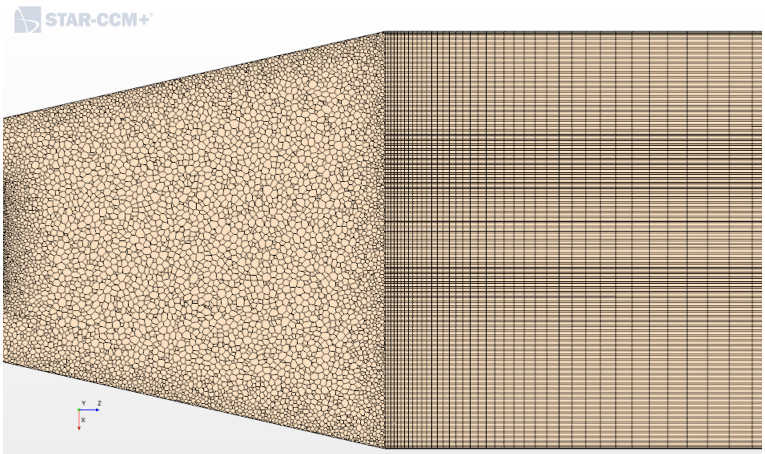

(b) Extruded mesh

Figure 4.9: Mesh close up views

The other models selected for the Physics Continuum used for the transient simulation were the same as the ones reported previously in Figure 4.2. Nevertheless, for this case a precursor RANS simulation has been performed in order to initialize the transient run such as to increase the convergence speed. For the RANS simulation the models selected for the Physics Continuum have been reported in Figure 4.10. The default setting has not been changed for the RANS models while for the transient run the same modifications described in section 4.1 has been applied.

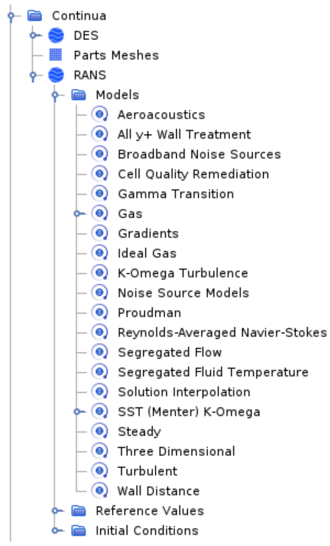

Figure 4.10: Models selected for the Physics Continuum used for the precursor RANS simulation

In order to reproduce the experimental results 7 microphones have been placed at the location specified in Figure 4.6 and the mean velocity vector has been computed by creating a vector user defined field function where each component were imposed as the mean of each velocity component. For this purpose three field mean monitor had to be generated each of which computed the average of the velocity field in x,y and z direction. In addition, also a scalar field function to compute the pressure fluctuations was created. This can be made simply by subtracting from the pressure its field mean.

Concerning the boundary conditions, the pipe inlet has been defined as Free Stream such as to avoid any spurious reflection. Here the Mach number has been specified as 0.0216 which corresponds to the 7.5 m/s inlet velocity imposed during the experiment. The surfaces composing the pipe and the flap have all been assigned to the Wall boundary condition. All the other surfaces have been defined as Pressure Outlet with the Unsteady Non-Reflecting Option activated. Nevertheless, this option becomes available only when an unsteady model has been selected for the Physics Continuum. Therefore, when performing the precursor RANS simulation the Unsteady Non-Reflecting Option could not be activated. Nevertheless, this option becomes available and has to be switched on when setting up the DES simulation, otherwise spurious sound reflections will be generated from the Pressure Outlet boundaries.

Once the precursor RANS simulation has been made run for 2000 iterations, the transient simulation has been started using $3 \cdot 10^{-5}$ s for the time step and the 2nd-order temporal discretization scheme.

In Figure 4.11 the velocity magnitude and pressure fluctuations obtained from the DES simulation have been reported in a scene covering nearly all the computational domain. The classical behaviour of the turbulent jet expanding in the open atmosphere can clearly be recognized. In addition, it is interesting to note how the pressure fluctuations have decreased considerably closer to the Pressure Outlet boundaries. Since the reflected flow unsteadiness are being dissipated also on the way back towards the microphones, it can be inferred that the influence of the reflection on the final results will be negligible.

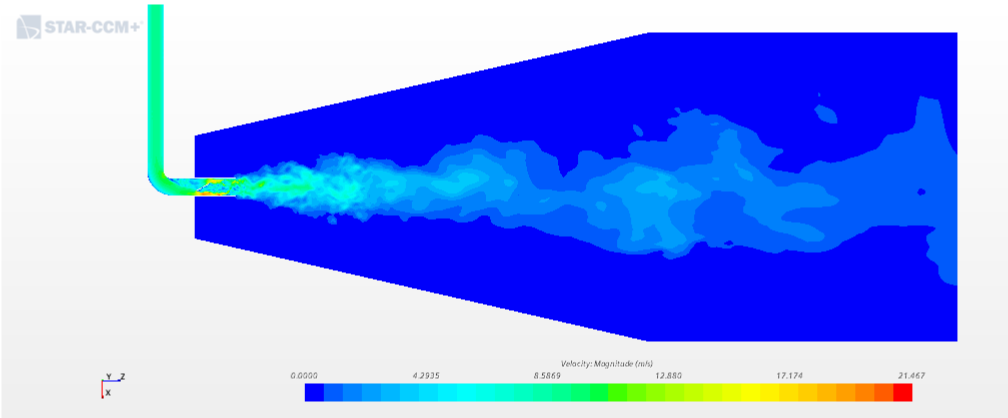

(a) Velocity magnitude

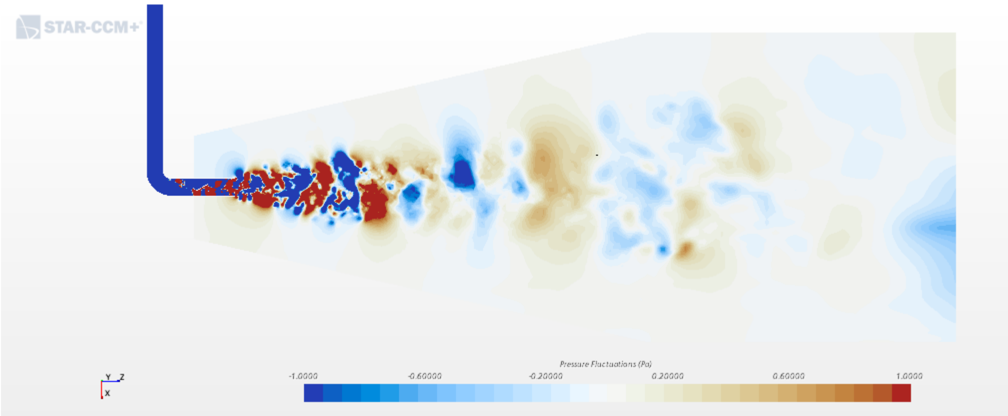

(b) Pressure Fluctuations

Figure 4.11: Visualization of the general behaviour of the flow over nearly the entire computational domain

Finally the simulations results have been compared with the available experimental data. In Figure 4.12 the comparison of the mean velocity vectors projected on the section $y = 0$ has been reported. The white spots visible in Figure 4.12a at the leading edge of the flap and inside the separation region after the bend are simply areas where the PIV measurements were not reliable enough due to optical difficulties such as shadow or reflections. Despite these white spots, it seems that the results obtained from the simulation agree quite well with the experimental data.

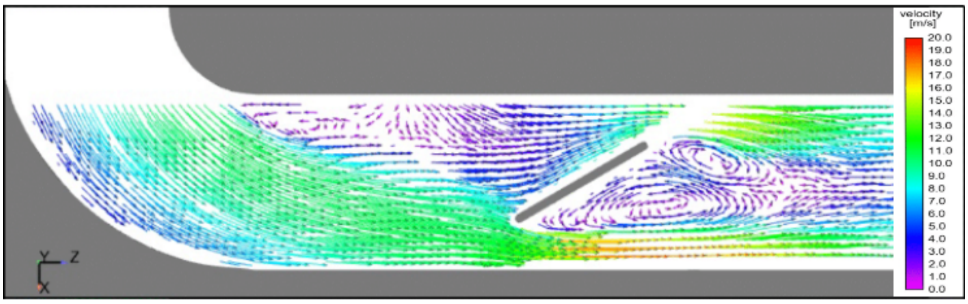

(a) PIV experiment results

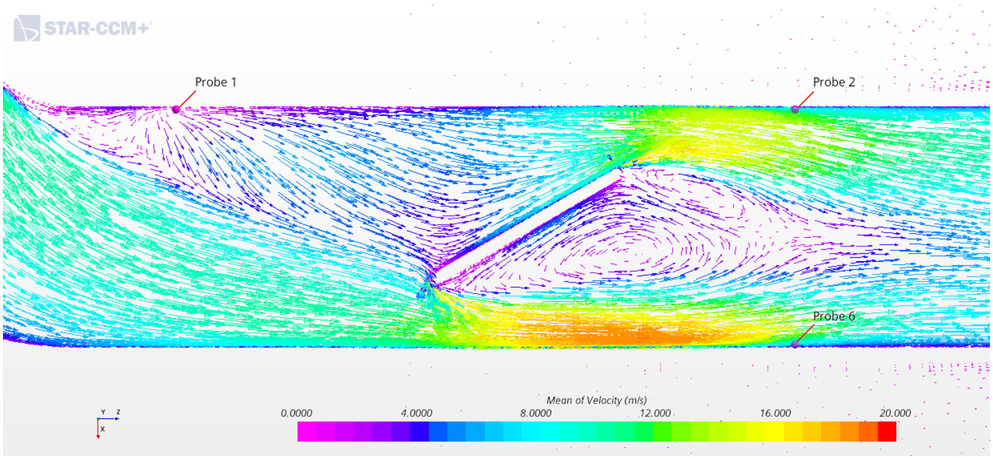

(b) Simulation results

Figure 4.12: Comparison of mean velocity vectors projected on section $y = 0$

Parameter	Setting
DFT-samples	512
Window	Hanning
Overlap	50%
Sampling frequency	2048 Hz
Frequency resolution	4 Hz

Table 4.2: Parameters employed for the Discrete Fourier Transform (DFT) performed on the pressure signal

In fact the two separation regions which occur after the flap and the 90° bend are very similar both in shape and size. In additions also the magnitude of the velocity vector as well as the angle of attack at the leading edge of the flap seems to relate quite well to the experimental measurements. Even though by looking closer to the pictures some small difference can be found, overall it can be concluded that the simulation methodology developed is able to predict the average behaviour of the flow field accurately.

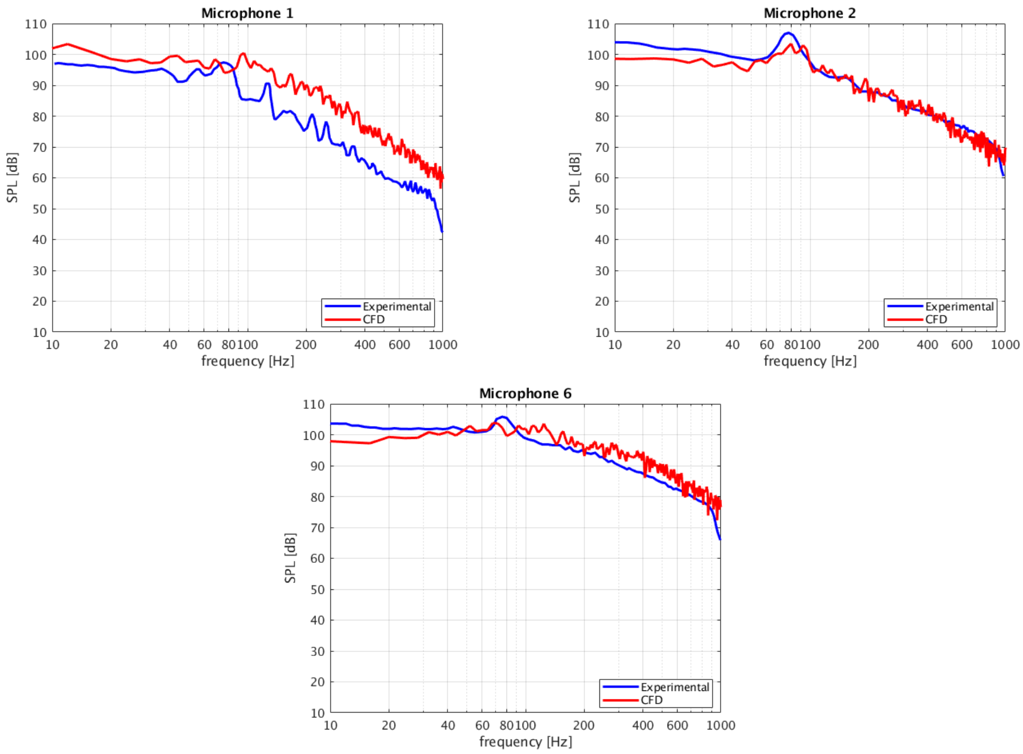

Figure 4.13: Comparison of wall pressure signal for three microphones location

In Figure 4.13 the comparison of the wall pressure fluctuations measured at the location of the 3 microphones highlighted in Figure 4.12 have been reported. Since the frequency analysis performed on the experimental pressure signal employed the parameters reported in Table 4.2, the pressure signal recorded during the simulation had to be post-processes accordingly. For this purpose the Matlab code reported in Appendix C has been developed. Overall an acceptable level of agreement has been obtained concerning both the trends of the curves and the pressure level predicted. Nevertheless, for microphone 6 the hump around 80 Hz, that is clearly visible for microphones 2, does not seem to be really pronounced. The largest discrepancy is found for the higher frequencies of microphone 1. This is probably due to the location where this microphone is positioned. In fact, from Figure 4.12 it can be noted that this microphone is exactly inside a separated region where it is assumed that even a slight difference in the location of the probe could affect the results much more.

After the comparison of the experimental data with the simulations results it can be stated that the simulation method employed is able to predict at an acceptable level of accuracy both the average flow field and the unsteady flow structures which are the sources of the aerodynamically generated noise. The next step would be to apply a similar method for the analysis of the acoustic characteristics of a real silencer geometry.

Chapter 5

Real Silencers Simulations

In the previous chapter it has been shown that the simulation methodology employed is able to predict acoustics quite accurately for relatively simple geometries. Here, real silencers configurations will be simulated using the same approach. The motivation behind these simulations comes from the results obtained from a recent experiment conducted by MAN Truck & Bus where it was found that flow-generated noise needed to be reduced drastically in order to satisfy commercial regulations. The test bench used for the experiment, which has been reported in Figure 5.1, consisted of a real truck and a microphone placed 0.5 meters away from the exhaust pipe exit section at an angle of 45°. The pillows positioned around both the exhaust pipe and the engine are needed in order to eliminate the structural noise generated by the vibrations.

Figure 5.1: Experimental setup used to measure the noise radiated from the exhaust system into the atmosphere, [23]

During the experiment the engine rpm was increased up until 2400 rpm and the spectrum was computed for different rpm values. In Figure 5.2 the obtained results have been reported. Even though some engine order content are still clearly visible at low rpm values, when the rpm is increased above approximately 1400 broadband flow-noise start to become dominant.

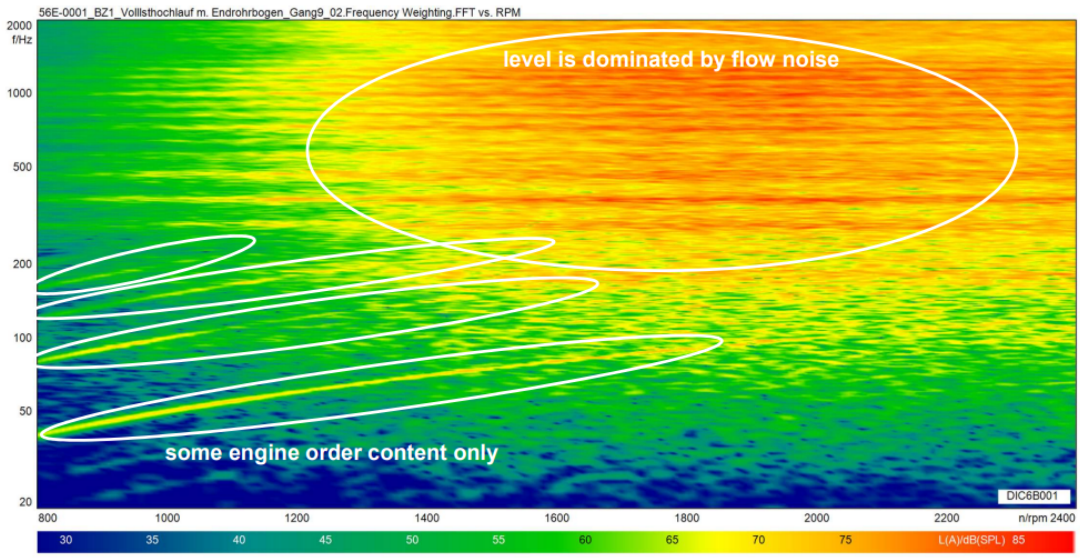

Figure 5.2: A-weighted SPL as a function of frequency and engine rpm, [23]

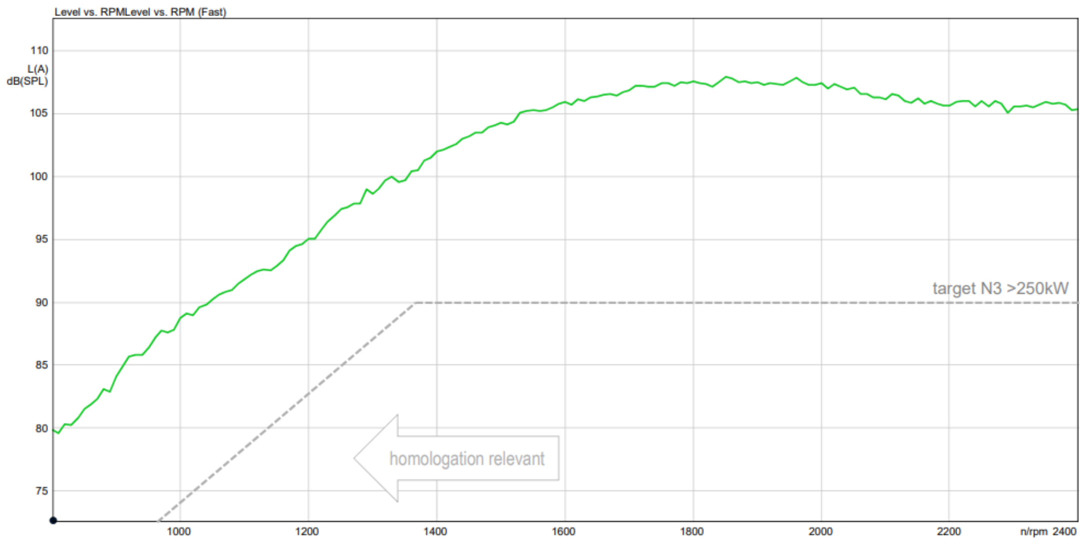

Figure 5.3: Overall A-weighted SPL as a function of the engine rpm, [23]

In Figure 5.3 the overall A-weighted SPL computed for the different engine rpm values has been reported as well. Here it can be seen that the noise radiated from the tested exhaust system is not able to meet the homologation target.

In this chapter, different configurations of the exhaust system will be analyzed by performing direct noise calculations in STAR-CCM+. First the simulation of the geometry used during the experiment will be performed such as to ascertain that the numerical results are close enough to the experimental measurements and to identify the main noise source regions. Finished this simulation other geometries will be analyzed in order to find possible solutions to attenuate flow-generated noise.

5.1 Simulation of the Experiment

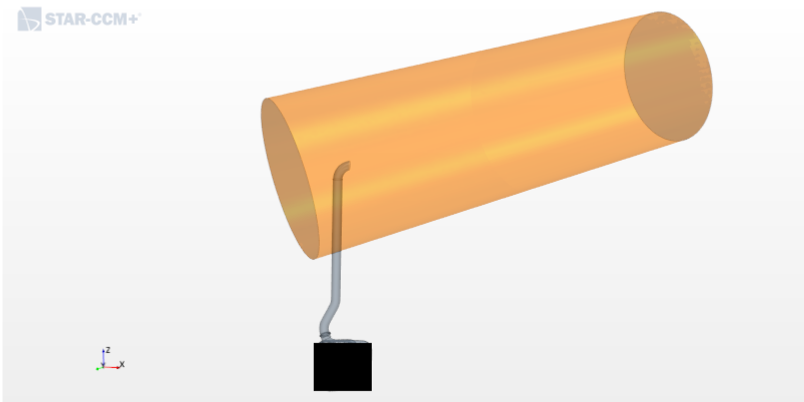

(a) View of the entire computational domain

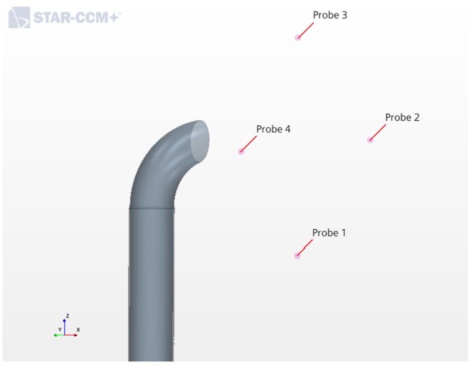

(b) Close up view on the exhaust pipe exit section

Figure 5.4: Representation of the geometry considered to simulate the experiment

In this section the simulation of the experiment just mentioned will be described. In Figure 5.4a the entire computational domain considered to replicate the experiment in STAR-CCM+ has been reported. This geometry has been imported as a surface mesh from a stl file generated in ANSA. The orange surfaces have all been specified as Pressure Outlet boundaries while the grey surfaces as Walls. Since Scania has asked not to release specific details regarding the silencer box geometry, a black square has been used to cover this part. Regarding the inlet flow boundary conditions it has been specified a mass flow rate of 2174.4 kg/hr and a total temperature of 332° C. These are the values that were measured during the experiment when the engine was operating at 2000 rpm. In Figure 5.4b the location of the simulated microphones have been reported. These microphones have all been placed 0.5 m away from the exit section of the exhaust pipe and at an angle of 45° such as to replicate the experiment set up. By analysing the experimental results it follows that the maximum frequency of interest is 2000 Hz. Therefore the cell size cannot be larger than $c/(20f_{max}) \approx 8$ mm if the sound is required to be calculated accurately at the location of the microphones.

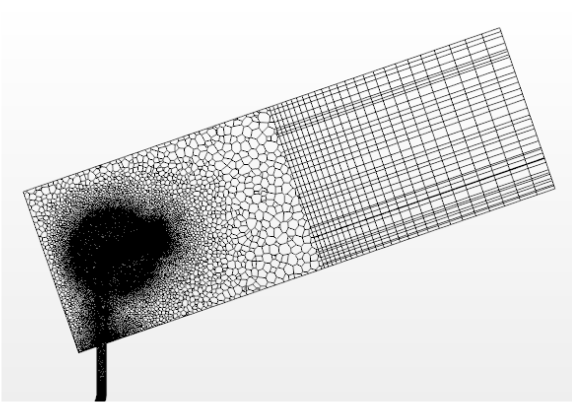

(a) Extruded mesh

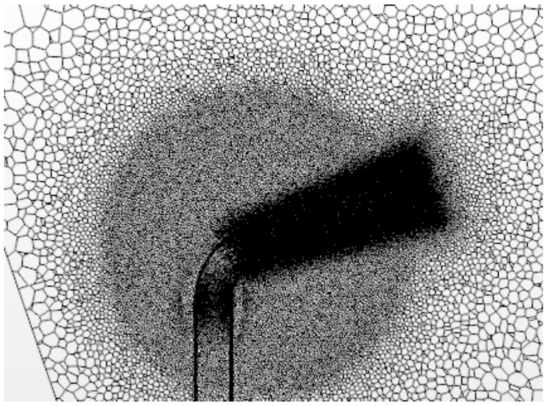

(b) Turbulent jet fine mesh

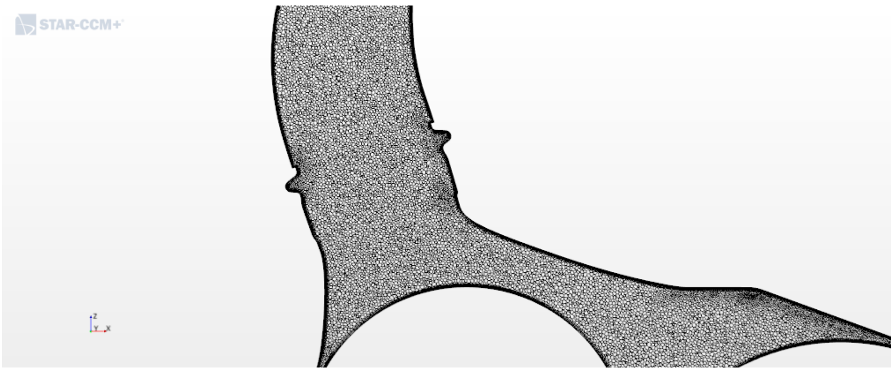

(c) Silencer fine mesh

Figure 5.5: Views of different mesh regions

Regarding the mesh, different views of the computational grid created have been reported in Figure 5.5. The first thing to be noted is that the polyhedral mesher has been used since it employs a robust algorithm which is known to yield good meshes even for complex geometries. In Figure 5.5a the extruded mesh generated through the Surface and Volume Extruder operations available in STAR-CCM+ can also be seen. This extruded region is 3 m long and is made of 25 layers with an initial wall thickness of 50 mm. With these settings, Appendix A yield a stretching factor between the cells of approximately 6.6% which is small enough to limit the occurrence of self-reflections. As a matter of fact, since in that region there will be the expanding turbulent jet, a flow velocity different than zero has to be expected and a stretching factor slightly bigger than 5% can be employed, see subsection 3.2.1.

In Figure 5.5b and Figure 5.5c close up views of the finer mesh regions have been reported. These are the regions were most of the flow-noise generating sources are located, namely the turbulent jet and the junction between the silencer and the exhaust pipe. In order to accurately capture the turbulent structures responsible for flow-noise generation the cell size has been limited to 2 mm in those regions.

Even though it is difficult to be perceived from the pictures reported in Figure 5.5, a prism layer has also been created for every surface specified as Wall boundary. This prism layer was made of 4 layers with a 1.1 stretching factor and 2.5 mm total thickness.

Once the computational domain has been created and the boundary conditions have been defined, the models for the physics continuum of the precursor RANS simulation have to be selected. For this simulation the same models that were shown in Figure 4.10 have been used. The steady state simulation has been run mainly to initialize the solution for the unsteady simulation and to check the mesh quality.

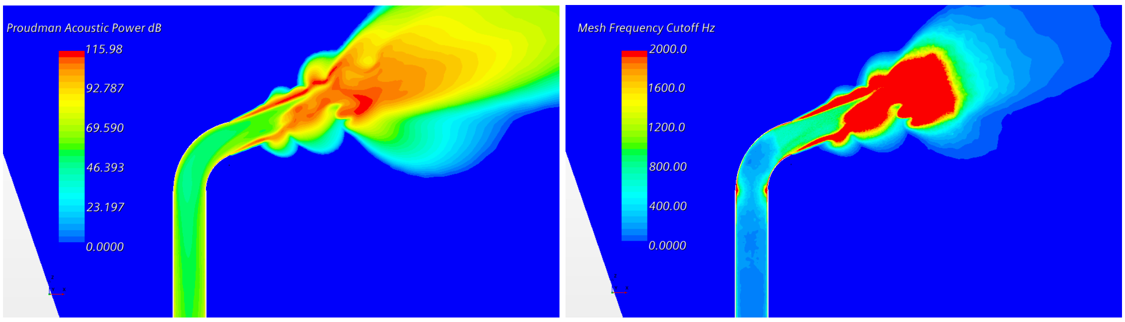

(a) Proudman Acoustic Power [dB] **(b)** Mesh Frequency Cutoff [Hz]

Figure 5.6: Plot of the Proudman Acoustic Power and Mesh Frequency Cutoff at the location of the exhaust pipe exit section

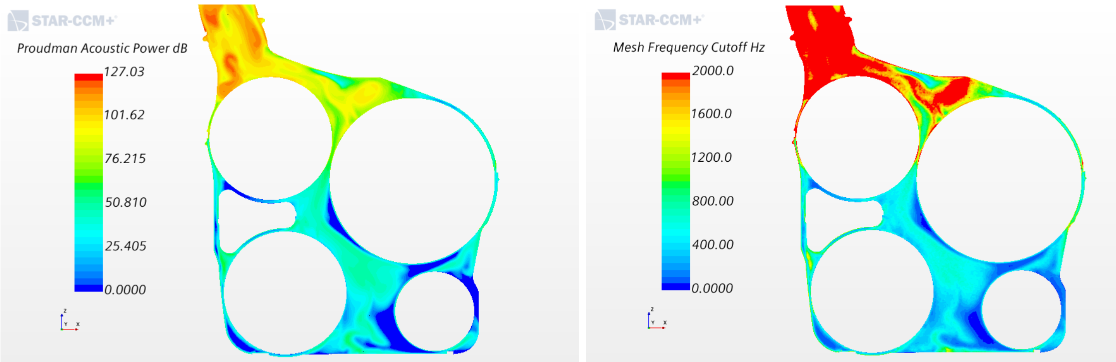

(a) Proudman Acoustic Power [dB]   **(b)** Mesh Frequency Cutoff [Hz]

Figure 5.7: Plot of the Proudman Acoustic Power and Mesh Frequency Cutoff at the location of the silencer

For this purpose, the RANS simulation has been first made run for 10000 iterations and then both the Proudman Acoustic Power and the Mesh Frequency Cutoff field functions have been plotted in a scene. These results can be seen reported in both Figure 5.6 and Figure 5.7, which show the regions where most of the flow-noise is being generated. It can be seen that the stronger noise sources are placed in the mixing region of the turbulent jet, outside of the potential core, and at the junction between the exhaust pipe and the silencer outlet. Then by analysing the maximum value reached by the Mesh Frequency Cutoff scenes it can be concluded that the cell size used is able to capture the noise-generating turbulent structures until 2000 Hz. Therefore, since this is the maximum frequency of interest, further mesh refinement is not needed in those regions.

Once the mesh quality has been ascertained, the DES simulation can be started using the results obtained from the RANS simulation as the initial condition. Regarding the physics continuum used to perform the DES simulation, the same models as shown in Figure 4.2 have been used. Concerning the Segregated Flow model, the Unsteady Flux Dissipation Corrections were enabled with the Limiting Acoustic-CFL set to 1. Furthermore the velocity and pressure under-relaxation factors have been limited to 0.8 and 0.5 respectively. These modifications to the setting employed in section 4.1 have been required since otherwise a problem known as odd-even decoupling were found to occur. The DES simulation has been made run for 1 s. The first 0.2 s was used to flush out all the initial transient artifacts and stabilize the flow, the remaining time was used to gather enough sampling data to be used in the post-processing of the results. In Figure 5.8 an overview of the behaviour of the turbulent jet generated at the exit of the exhaust pipe has been reported. From the scene where the pressure fluctuations are plotted it can be seen that the wave fronts initially start as spherical near the pipe exit. In addition, it can also be inferred how much the flow unsteadiness is being reduced towards the boundaries, leading to a small impact of the reflections on the final results. In both pictures it has also been highlighted the location of one of the microphones used to sample the data. Being placed outside of the turbulent jet no hydrodynamic fluctuation will be measured but only the sound pressure fluctuations.

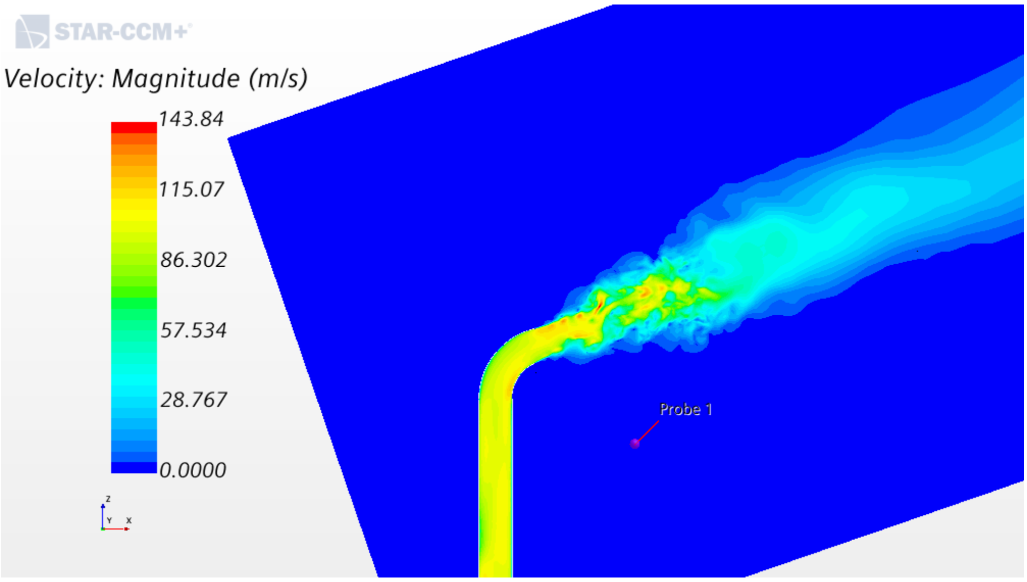

(a) Velocity Magnitude [m/s]

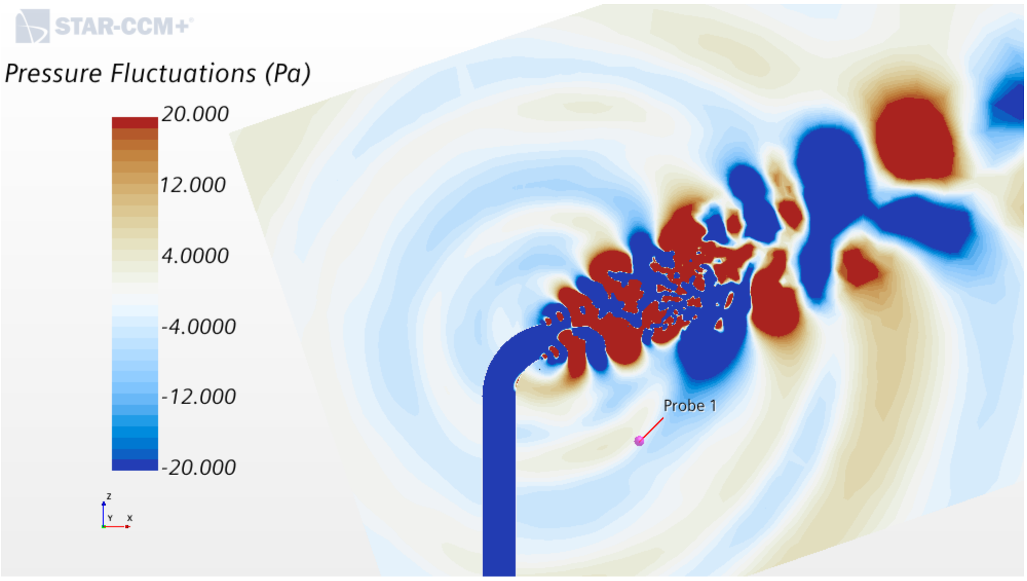

(b) Pressure Fluctuations [Pa]

Figure 5.8: General behaviour of the turbulent jet at the exit of the exhaust pipe

In Figure 5.9 it has been reported the A-weighted SPL as measured by the highlighted microphone. If these results are compared to the experiment data reported in Figure 5.2 when the engine is at 2000 rpm, a quite good agreement can be observed.

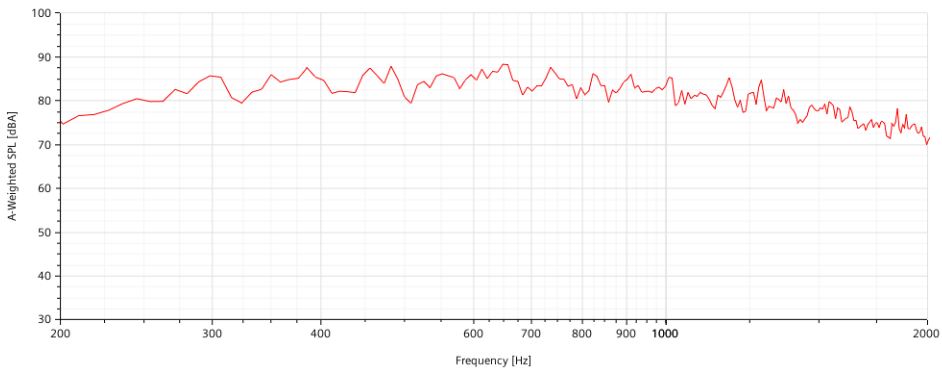

Figure 5.9: A-weighted SPL plot computed in STAR-CCM+

The calculation of the A-weighted SPL has been carried out in STAR-CCM+ by creating a Data Set Functions > Point Time Fourier Transform with the parameters specified in Table 5.1. The lower frequency plotted in Figure 5.9 has been limited only to 200 Hz because both the sampling time and the length of the computational domain were not considered to be large enough to capture lower frequencies properly. Nevertheless, most of the noise was concentrated in the frequency range plotted. Then by computing the integral of the spectrum the OASPL can be obtained. The simulation has yielded an OASPL equal to 105.1 dBA while from the experiment results reported in Figure 5.3 it can be extracted that at 2000 rpm the OASPL was equal to 107.4 dBA. This slight underestimation is thought to be reasonable since in the experiment the noise produced by the engine and other parts is also included.

Property	**Setting**
Start Time	0.2 s
Cut-off Time	1 s
Amplitude Function	A-Weighted SPL
Frequency Function	Frequency
Analysis Blocks	7
Overlap Factor	0.5
Window Function	Hamming

Table 5.1: Properties settings employed for the calculation of the A-weighted SPL in STAR-CCM+

5.2 Different Silencer Configurations

As it has been shown both in Figure 5.6 and Figure 5.7 the two main sources of flow-generated noise are located in the mixing layer, between the potential core of the turbulent jet and the atmosphere, and at the junction between the exhaust pipe and the silencer box. Therefore, a modification of the geometry in these region could have a great impact on the noise radiated from the exhaust system. For this purpose, the different configurations reported in Figure 5.10 have been simulated using the same method described in the previous section. Both the MAN Box and the Scania Box have been hidden by a black square because Scania has asked not to disclose the details of the silencer box. The results obtained for the five different exhaust system configurations simulated will be shown and compared in this section.

MAN Pipe + MAN Box is similar to the configuration that was analyzed in the previous section but the length of the pipe is a bit shorter.

The 2 Box Pipe geometry has been generated by cutting the termination of the MAN Pipe with an oblique plane such as to obtain an elliptic exit section. In fact it was thought that by increasing the area of the pipe exit cross section the turbulent jet Mach number would have been reduced and thus the noise level.

Similarly, also the Chevron Pipe has been made with a larger exit cross section than the MAN Pipe. Therefore, a certain level of noise attenuation was expected also for this geometry. In addition, the wavy contour should serve to develop the turbulent jet more gradually and possibly to further reduce the noise radiated. As a matter of fact, chevrons nozzles have been widely used on turbofan engines due to their beneficial effects on noise attenuation. Nevertheless the phenomenon that is responsible for this noise attenuation is not exactly understood yet.

Another interesting configuration that has been simulated is the Perforated Pipe. In this case the same geometry of the 2 Box Pipe has been used, but the termination of the pipe has been perforated using multiple circular holes. This configuration should allow some of the flow to escape from the holes, thus reducing the Mach number of the turbulent jet. In addition noise attenuation could be even further increased due to the absorption of acoustic energy caused by the additional vortex shedding from the rim of each hole, [24].

The last geometry analysed was made of the MAN Pipe + Scania Box. The Scania Box differs from the MAN Box because the junction between the silencer and the exhaust pipe has been moved from the edge of the box towards the middle. This modification to the silencer box was thought to affect positively the acoustic performance of the exhaust system. As a matter of fact, moving the junction of the pipe near the middle of the box should leave the flow more space to exit from the silencer. This eventually should lead to smaller Mach numbers at the junction with the pipe, thus decreasing the noise level.

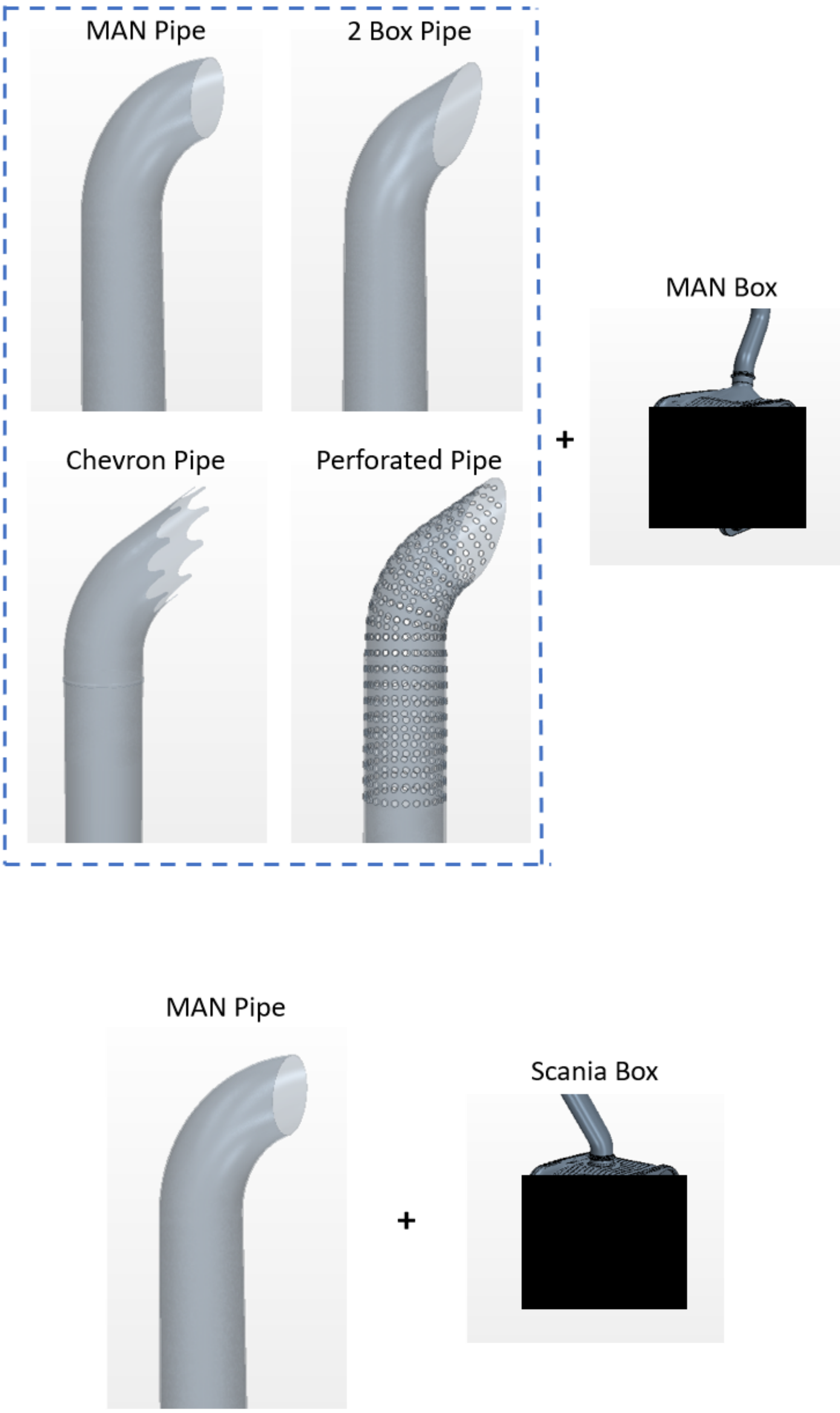

Figure 5.10: Different silencer configurations simulated

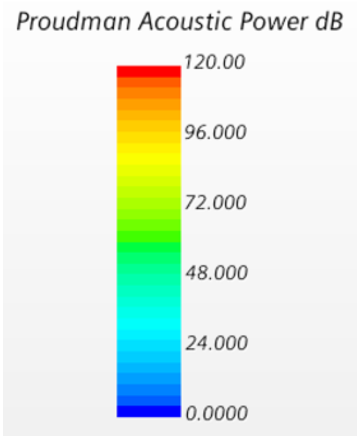

Figure 5.11: Reference color bar for the Proudman acoustic power scenes reported in Figure 5.12

For the simulation of all these geometries the same procedure described in section 5.1 has been followed. Nevertheless, since no experimental results were available the inflow conditions have been changed. Namely, the mass flow rate has been set to 1850 kg/hr and the total temperature to 450° C. These are the standard values used at Scania when performing pressure drop simulations.

After the precursor RANS simulation has finished to run for each of the silencer configurations the Proudman acoustic power has been compared in Figure 5.12. For all these images the color bar shown in Figure 5.11 should be used as reference. By analysing the Proudman acoustic power scenes, the biggest difference has been found only for the Perforated Pipe configuration. Here it has been obtained that the flow-noise sources are a bit more spread around the exhaust pipe outlet and the strength of these sources seem to be reduced.

Then, after the DES simulations have been performed for each geometry, the noise spectrum can be computed by post-processing the pressure data monitored by the microphone placed close to the outlet pipe. In Figure 5.13 the spectrum computed using the same parameters reported in Table 5.1 has been reported for each of the configurations simulated. In order to ease the comparison the Overall A-weighted Sound Pressure Level (OASPL) has been computed as well. This parameter is calculated using the following equation:

$$OASPL = 10\log_{10}\left(\sum_{i=1}^{n} 10^{SPL_{A_{f_i}}/10}\right) \tag{5.1}$$

where f_i identify the A-weighted SPL value associated to the i-th frequency reported in the spectrum. Equation 5.1 has been implemented in Matlab and the values of the spectrum generated in STAR-CCM+ have been used for the computation of the OASPL.

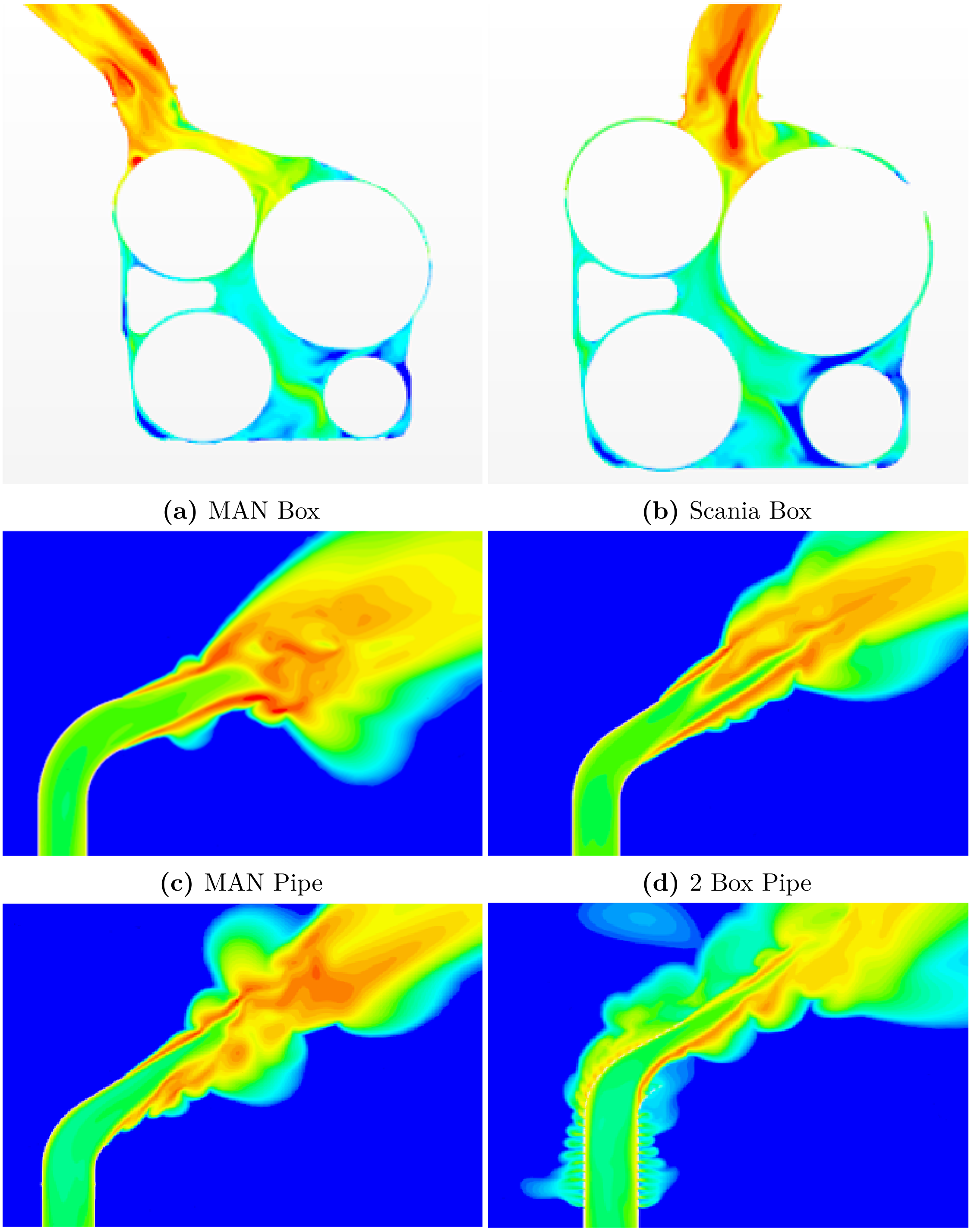

(a) MAN Box

(b) Scania Box

(c) MAN Pipe

(d) 2 Box Pipe

(e) Chevron Pipe

(f) Perforated Pipe

Figure 5.12: Scenes of the Proudman Acoustic Power obtained for the different silencer configurations simulated

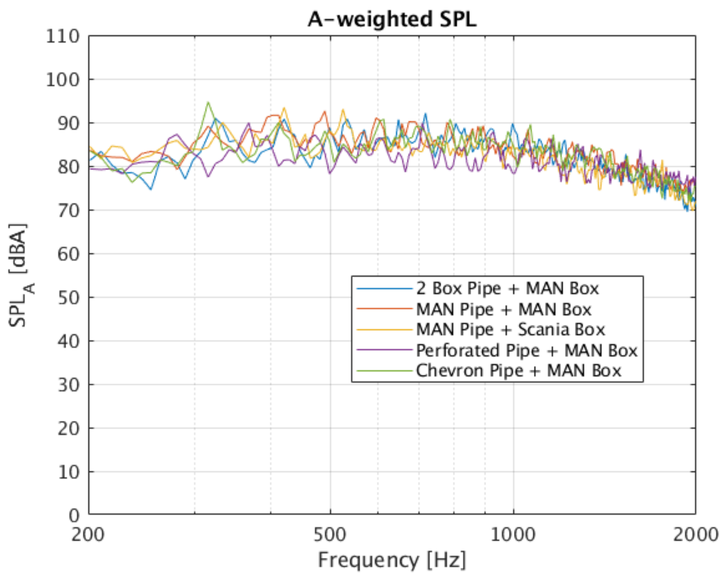

Figure 5.13: Spectrum of the five different silencer configurations analysed

The comparison between the obtained OASPL values has been reported in Table 5.2. By analysing these values, it has been found that the highest level of noise has been produced by the MAN Pipe + MAN Box configuration. For all the other configurations simulated a lower noise level has been obtained. In particular with the Perforated Pipe + MAN Box the highest noise attenuation has been found. Nevertheless, it has to be noted that even by replacing the MAN Box with the Scania Box has reduced the noise level considerably. Therefore, it can be imagined that a combination of Perforated Pipe + Scania Box would attenuate the noise level even further. Nevertheless, this configuration has not been simulated. As a matter of fact, since the silencer box is constrained by other components, it is easier to apply modification to the pipe outlet.

Configuration	**OASPL**
MAN Pipe + MAN Box	107.75 dBA
2 Box Pipe + MAN Box	107.11 dBA
Chevron Pipe + MAN Box	107.2 dBA
Perforated Pipe + MAN Box	105 .15 dBA
MAN Pipe + Scania Box	106.41 dBA

Table 5.2: Comparison of the OASPL obtained for the different silencer configurations simulated

Therefore the focus has been centered on the reduction of flow noise yielded by a modification of the outlet pipe geometry and not the silencer box. Nevertheless, it is interesting to note that the outlet of the silencer box has a significant impact on the noise level and an improved design of this part could also lead to improve the acoustics performance of the exhaust system.

In conclusion, from the obtained results it can be inferred that flow-noise attenuation is generally achieved with a reduction of the flow Mach number. As a matter of fact, even the Perforated Pipe can be seen as an increase of the outlet pipe area since the average flow velocity is decreased at the pipe exit cross section due to some of the flow escaping from the holes. Nevertheless, even if noise attenuation was the biggest concern during this thesis work, there could be other considerations that would make the different silencer configurations proposed not applicable in real life. For example, in case of heavy rain conditions it could be that a lot of water would enter inside the silencer if the exhaust pipe is perforated. Since this would not be acceptable, it should be ascertained that this problem does not occur. However, the study of this problem is outside of the scope of this thesis work, the aim of which was to demonstrate the feasibility of accurate aeroacoustic simulations in STAR-CCM+ and to propose possible solutions for noise attenuation.

Chapter 6

Conclusions

Throughout this report it has been shown that the use of STAR-CCM+ to perform direct noise calculations yield quite accurate and realistic results. In particular the simulation method studied during the development of this thesis has been applied both on simple and complex exhaust system geometries and for all the simulation performed a reasonable level of agreement has been obtained with the experimental results available.

The biggest limitation associated to the application of the simulation methodology employed throughout this thesis is the quite high computational time required. As a matter of fact, in order to perform one simulation of the five silencer configurations described in section 5.2, 1000 cores of the Scania cluster were used. Despite the high computational power used, approximately five days were still required to perform each of the simulations. Therefore, when this simulation method is employed much care should be appointed to keep the computational domain as small as possible.

Another important recommendation that is worth to mention is the limitation of the application of this method to flows with a Mach number lower than approximately 0.3. Otherwise compressible flow effects, such as shock waves, should be taken into account and the Ideal Gas flow assumption would decay.

Nevertheless, if the limitations just presented are not ignored, with this report it has been proven that with the application of the direct noise calculation method described in this thesis work valuable information on the acoustic characteristics of flow can be captured. As a matter of fact, from the comparison of the results reported in section 5.2, it has been possible to find the main flow-noise sources within the exhaust system and identify the silencer configuration which generate the least amount of flow-noise. In particular it has been concluded that the Perforated Pipe termination could have a significant effect on flow-noise attenuation. Therefore it would be interesting to perform an experiment on this configuration and see if similar results are obtained.

6.1 Ideas for Future Work

Here below there have been reported two ideas which could be considered to further develop the thesis work described in this report.

- The Transmission Loss (TL) is a very common parameter which is often used to characterize the acoustic performance of a silencer. In section 4.1 it was shown that the TL could be computed easily using the decomposition method. Nevertheless, if flow generated noise were to be considered, this method is not applicable anymore. In fact, the decomposition method can not include the noise generated from the free turbulent jet exiting from the exhaust pipe. Therefore, it would be interesting to find a different approach which would include also the flow-generated noise in the calculation of the total radiated acoustic power. In [25] it has been found an experimental set up which compute the total radiated sound power in the far field by summing the products of sound intensities measured by different microphones and the corresponding elemental areas. The microphones were placed on a large sphere around the pipe exit section such as not to include the hydrodynamic fluctuations in the calculations. This seems a promising approach which could be tried to be replicated in a simulation such as to have a method that can be used also for the computation of the TL when flow-generated noise need to be taken into account.
- From the comparison of the different silencer configurations reported in section 5.2, it was found that with the Perforated Pipe the least amount of noise was obtained. Nevertheless, since this conclusion is not supported by any experimental evidence, the Perforated Pipe should be tested before declaring the obtained results with absolute certainty. In addition this would be an opportunity to further validate the simulation method used throughout this thesis work. Then this method could be also used for the optimization of the Perforated Pipe geometry by analysing the influence of different parameters such as the spacing, the diameter and the number of holes.

Appendix A

Matlab code used for the determination of the stretching factor for an extruded grid generated in STAR-CCM+. The initial wall thickness, the number of layers and the extrusion distance are parameters that have to be set by the user.

```

clear all
close all
clc

% fsolve starting value
X0 = 1.1;
% Equation to solve
FUN = @(str) find_str(str);

% X = grid stretching
% FVAL = FUN(X) (FVAL should be close to zero)
[X,FVAL] = fsolve(FUN,X0)

function [res] = find_str(str)

% Initila Wall Thickness in meters
t = 0.01;
% Extrusion Distance in meters
T = 1.5;
% Number of Layers
n = 40;

length = ones(1,n);
```

```
for i=1:n
    length(1,i) = str^(i-1);
end

% sum(length) is the sum of the thickness of
% each layer of the extruded grid
res = T-t*(sum(length));

end
```

Appendix B

Matlab code used for the analysis of the simple muffler configurations. The first part is used to generate the inlet noise signal to be imported in STAR-CCM+. The second is the implementation of the decomposition method for the computation of the transmission loss.

```
clear all
close all
clc

%% Generate Inlet Noise Signal

% Time step
dt = 2.5e-5;
% Time period
T = 0.4;
t = 0:dt:T;
% Frequency range
f = 500:5:1500;
N_f = length(f);
% Phase shift
phi = rand(N_f,1);

fun = zeros(length(t),1);

for i=1:length(t)
    for j=1:N_f

        fun(i) = fun(i) + 0.00001*(sin(2*pi*(f(j)*t(i)+phi(j))));
```

```
    end
end

% Inlet noise signal plot
figure(1)
plot(t,fun);
xlabel('time [s]')
ylabel('M [-]')
title('Inlet Noise Signal')
xlim([0,0.03])
grid on

% Write file to be exported in STAR-CCM+
cHeader = {'time' 'Mach'};
commaHeader = [cHeader;repmat({','},1,numel(cHeader))];
commaHeader = commaHeader(:)';
textHeader = cell2mat(commaHeader);
textHeader = textHeader(1:end-1);
fid = fopen('Inlet_Noise.csv','w');
fprintf(fid,'%s\n',textHeader);
fclose(fid);
dlmwrite('Inlet_Noise.csv',[t',fun],'-append');

%% Decomposition Method

% Geometry
D1 = 48.59e-3;
D2 = 153.18e-3;
S1 = pi*D1^2/4;
S2 = pi*D2^2/4;
l = 540e-3;

% Import pressure signal monitored by STAR-CCM+
T1 = readtable('P1.csv');
T2 = readtable('P2.csv');
T3 = readtable('P3.csv');
A1 = table2array(T1);
A2 = table2array(T2);
A3 = table2array(T3);
```

```
L = length(A1(:,2));
% Time step
dt = (A1(2,1)-A1(1,1));
% Sampling frequency
fs = dt^-1;
% Distance between microphone 1 and 2
s_12 = 100e-3;

% Compute auto and cross spectrum
[S11,f1] = periodogram(A1(:,2),hamming(L),L,fs);
[S22,f2] = periodogram(A2(:,2),hamming(L),L,fs);
[S33,f3] = periodogram(A3(:,2),hamming(L),L,fs);
[S12,f12] = cpsd(A1(:,2),A2(:,2),hamming(L),[],L,fs);

ks_12 = 2*pi*f1/c*s_12;

% Compute auto spectrum incident wave
NSaa = (S11+S22-2*real(S12).*cos(ks_12)+2*imag(S12).*sin(ks_12));
DSaa = 4*sin(ks_12).^2;
Saa = NSaa./DSaa;

% Compute incident and transmitted effective sound pressure
P_in = sqrt(abs(Saa));
P_tr = sqrt(abs(S33));

% TL computed according to decomposition method
TL = 20*log10(P_in./P_tr);
% TL computed with analytical formula
TL_a = 10*log10(1+1/4*(S1/S2-S2/S1)^2*sin(2*pi*f1/c*l).^2);

% Plot both TL for comparison
figure(1)
plot(f1(1:2:end),TL(1:2:end),f1(1:2:end),TL_a(1:2:end),'LineWidth'
    ,2)
hold on

% Add TL from experiment
fileID = fopen('Exp1.txt','r');
formatSpec = '%f %f';
sizeA = [2 Inf];
A = fscanf(fileID,formatSpec,sizeA);
```

```
plot(A(1,:),A(2,:),'LineWidth',2);
plot(f_max*ones(1,22),0:1:21,'--k')

xlim([500,1500])
ylim([0,20])
legend('CFD','Analytical Formula','Experimental Results','location',
    ↪ 'best')
xlabel('f [Hz]')
ylabel('TL [dB]')
grid on
hold off
```

Appendix C

Here it has been reported an adaptation of the Matlab code found in [26], which has been used to perform the post-processing of the unsteady pressure signal obtained from the simulation described in section 4.2.

```
clc
clear
close all

% Load simulation data
file_data = importdata('Validation_Probe2.csv');
data = file_data.data;
time = data(:,1);
sig = data(:,2);

% Load experimental data
file_data_exp = importdata('SPL2_dot.txt');
f_exp = file_data_exp(:,1);
SPL_exp = file_data_exp(:,2);

% Resampling frequency
NN = 2048;
% FFT points
NFFT = 512;
Ts = 1/NN;
fs = 1/Ts;
sig0 = sig;
time0 = time;
time = time0(1):Ts:time0(end);
```

```
% Resample the pressure data
sig = interp1(time0,sig0,time,'spline');

% Plot pressure in time domain
figure(1)
plot(time,sig);
axis([min(time) max(time) -80 80])
title('pressure');
xlabel('time [s]');

% Select NN points
sig = sig(end-NN+1:end);

% Compute fluctuating component
sig_fluct = sig-mean(sig);

% Compute power spectral density of the signal
[psd,f]=pwelch(sig_fluct,hanning(NFFT,'periodic'),NFFT/2,NFFT,fs);

% Frequency resolution
df = f(2)-f(1);

% Reference pressure [Pa]
p_ref = 2e-5;

% Compare simulation with experiment SPL
figure(2)
SPL = 10*log10(psd.*df./(p_ref.^2));
semilogx(f_exp, SPL_exp,'b',f,SPL,'r','LineWidth',2)
axis([10 1000 10 110])
legend('Experimental','CFD','Location','best')
set(gca,'XTick',[10 20 40 60 80 100 200 400 600 1000 2000]);
xlabel('frequency [Hz]');
ylabel('SPL [dB]');
title('Microphone 2');
grid on
```

Bibliography

[1] D. Jhanwar. «Noise Pollution: A Review». In: *Journal of Environment Pollution and Human Health* 4.3 (2016), pp. 72–77 (cit. on p. 1).

[2] N. Pignier. *The impact of traffic noise on economy and environment: a short literature study*. The Centre for ECO^2 Vehicle Design, KTH Aeronautical and Vehicle Engineering, 2015 (cit. on p. 1).

[3] C. D. Francis, C. P. Ortega, and A. Cruz. «Noise Pollution Changes Avian Communities and Species Interactions». In: *Current Biology* 19.16 (Aug. 2009), pp. 1415–1419 (cit. on p. 1).

[4] World Health Organization - Regional Office for Europe. *Environmental Noise Guidelines for the European Region*. 2018 (cit. on p. 2).

[5] T. Jonas, P. Garcia, and C. Kuntz. «Shell noise from car exhaust system». In: *25th FISITA Congress*. Beijing, China, Oct. 1994, pp. 204–210 (cit. on p. 3).

[6] N.J. Pignier, C.J. O'Reilly, and S. Boij. «Aerodynamic and aeroacoustic analysis of a submerged air inlet in al low-Mach-number flow». In: *Computer & Fluids* 133 (July 2016), pp. 15–31 (cit. on p. 3).

[7] F.T.M. Nieuwstadt, B.J. Boersma, and J. Westerweel. *Turbulence: Introduction to Theory and Applications of Turbulent Flows*. Springer, 2016 (cit. on pp. 7, 13).

[8] D.C. Wilcox. *Turbulence Modeling for CFD*. DCW Industries, 2006 (cit. on p. 11).

[9] S. Hickel. *Slides for the course AE4202 CFD for Aerospace Engineers*. Delft University of Technology. 2020 (cit. on p. 11).

[10] D.C. Wilcox. «Re-assessment of the scale-determining equation for advanced turbulence models». In: *AIAA Journal* 26.11 (1988), pp. 1299–1310 (cit. on p. 11).

[11] F. R. Menter. «Two-Equation Eddy-Viscosity Turbulence Models for Engineering Applications». In: *AIAA Journal* 32.8 (Aug. 1994), pp. 1598–1605 (cit. on p. 12).

[12] `https://physics.stackexchange.com/questions/281281/about-the-definition-of-boundary-layer` (cit. on p. 13).

[13] D. G. Simons. *Reader for the course AE4431 Aircraft Noise and Emissions.* Delft University of Technology. 2019 (cit. on pp. 14, 16–19, 23).

[14] M. J. Lighthill. «On Sound Generated Aerodynamically. I. General Theory». In: *Proceedings of the Royal Society of London A: Mathematical, Physical and Engineering Sciences* 211.1107 (Mar. 1952), pp. 564–587 (cit. on p. 21).

[15] N. Curle. «The Influence of Solid Boundaries upon Aerodynamic Sound». In: *Proceedings of the Royal Society A: Mathematical, Physical and Engineering Sciences* 231.1187 (Sept. 1959), pp. 505–510 (cit. on p. 22).

[16] J.E.F. Williams and D.L. Hawkings. «Sound Generation by Turbulence and Surfaces in Arbitrary Motion». In: *Philosophical Transactions of the Royal Society A: Mathematical, Physical and Engineering Sciences* 264.1151 (May 1969), pp. 1–32 (cit. on p. 22).

[17] P.R. Spalart, W. H. Jou, M. Strelets, and S.R. Allmaras. «Comments on the feasibility of LES for wings, and on a hybrid RANS/LES approach». In: *Proceedings of the First AFOSR International Conference on DNS/LES* (Aug. 1997) (cit. on p. 27).

[18] Adam Sandström. «Simulating flow-noise for after-treatment systems». MA thesis. KTH Royal Institute of Technology, 2020 (cit. on pp. 30, 33, 36, 50).

[19] J. Middelberg, T.J. Barber, S. Leong, K.P. Byrne, and E. Leonardi. «Computational Fluid Dynamics Analysis of the Acoustic Performance of Various Simple Expansion Chamber Mufflers». In: *Proceedings of Acoustics* (2004) (cit. on pp. 42, 43).

[20] Z. Tao and A. Seybert. «A Review of Current Techniques for Measuring Muffler Transmission Loss». In: *Proceedings of the SAE Noise Vibration Conference and Exhibition* (2003) (cit. on p. 45).

[21] A.F. Seybert. «Two-sensor methods for the measurement of sound intensity and acoustic properties in ducts». In: *The Journal of The Acoustical Society of America* 83.6 (June 1988), pp. 2233–2239 (cit. on p. 45).

[22] A. Jäger et al. «Numerical and experimental investigation of the noise generated by a flap in a simplified HVAC duct». In: *AIAA Paper 2008-2902* (May 2008) (cit. on pp. 47–49).

[23] Helmut Wiesbeck. *Exhaust Orifice Noise CAS-1 with Vertical Pipe.* MAN Truck Bus. 2020 (cit. on pp. 57, 58).

[24] M.S. Howe. «Attenuation of sound in a low Mach number nozzle flow». In: *Journal of Fluid Mechanics* 91 (1979), pp. 209–229 (cit. on p. 65).

[25] M. Salikuddin. «Acoustic Power Dissipation On Radiation Through Duct Terminations: Experiments». In: *Journal of Sound and Vibration* 91.4 (1983), pp. 479–502 (cit. on p. 72).

[26] Cong Wang. «Numerical Investigation of Flow Induced Noise in a Simplified HVAC Duct with OpenFOAM». MA thesis. KTH Royal Institute of Technology, 2013 (cit. on p. 79).